

Experimental Liouvillian exceptional points in a quantum system without Hamiltonian singularities

Shilan Abo¹, Patrycja Tulewicz¹, Karol Bartkiewicz¹, Şahin K. Özdemir², and Adam Miranowicz^{1†}

¹ Institute of Spintronics and Quantum Information, Faculty of Physics, Adam Mickiewicz University, 61-614 Poznań, Poland

² Department of Electrical and Computer Engineering, Saint Louis University, St. Louis MO 63103, USA

E-mail: adam.miranowicz@amu.edu.pl

Abstract. Hamiltonian exceptional points (HEPs) are spectral degeneracies of non-Hermitian Hamiltonians describing classical and semiclassical open systems with losses and/or gain. However, this definition overlooks the occurrence of quantum jumps in the evolution of open quantum systems. These quantum effects are properly accounted for by considering quantum Liouvillians and their exceptional points (LEPs). Specifically, an LEP corresponds to the coalescence of two or more eigenvalues and the corresponding eigenmatrices of a given Liouvillian at critical values of external parameters [Minganti *et al.*, Phys. Rev. A **100**, 062131 (2019)]. Here, we explicitly describe how standard quantum process tomography, which reveals the dynamics of a quantum system, can be readily applied to detect and characterize quantum LEPs of quantum non-Hermitian systems. We conducted experiments on an IBM quantum processor to implement a prototype model with one-, two-, and three qubits simulating the decay of a single qubit through competing channels, resulting in LEPs but not HEPs. Subsequently, we performed tomographic reconstruction of the corresponding experimental Liouvillian and its LEPs using both single- and two-qubit operations. This example underscores the efficacy of process tomography in tuning and observing LEPs even in the absence of HEPs.

† Author to whom any correspondence should be addressed.

1. Introduction

Systems with dissipation and/or amplification can be described by non-Hermitian Hamiltonians (NHHs) whose eigenvalues are either real or complex conjugate pairs depending on whether the system is operated in the exact or broken parity-time (\mathcal{PT}) symmetric phase, respectively [1, 2, 3]. Over the past two decades, \mathcal{PT} -symmetric systems have evolved from a mathematical curiosity to a powerful resource for controlling electromagnetic waves and their interactions with matter by judiciously engineering loss-imbalance in passive (i.e., without amplification) non-Hermitian systems, and dissipation vs amplification rates in active non-Hermitian systems, as well as dissipation vs the coupling strength between subsystems [4, 5]. Early demonstrations involved optical [6, 7, 8], electronic [9], plasmonic [10], metamaterial [11, 12, 13], optomechanical, and acoustic [14, 15, 16] systems, before further expanding to include other platforms [17, 18, 19, 20, 21, 22]).

The exact and broken \mathcal{PT} -symmetric phases are separated by the so-called Hamiltonian exceptional points (HEPs), where two or more of the eigenvalues of the effective NHH describing a given system, and their associated eigenvectors, become degenerate, leading to dimensionality reduction [23, 24, 25].

A plethora of intriguing properties of such systems induced or enhanced at HEPs (or near them) have been predicted, including stimulated [26, 27, 28, 29, 30, 31] and spontaneous [32] emission, chirality [33, 34, 35], unidirectional invisibility [36], control of whispering-gallery microcavities [37, 38], an exceptional Kerr effect [39] and related exceptional photon blockade [40], or the generation of higher-order HEPs [41, 42, 43, 44]. The existence of HEPs in the absence of the \mathcal{PT} -symmetry was studied in Ref. [45].

While effective NHHs and HEPs are sufficient to describe coherent nonunitary evolution of the dynamics of classical and semiclassical systems, they fell short in describing the evolution of quantum systems involving quantum jumps and associated noise. To address this shortcoming, quantum Liouvillian exceptional points (LEPs) were introduced as degeneracies of quantum Liouvillian superoperators associated with their coalescing eigenvalues and eigenvectors [46]. LEPs are a natural generalization of HEPs by including quantum jumps to provide a consistent description of decoherence and noise in open quantum systems compatible with the canonical commutation relations. Indeed, LEPs depend not only on a continuous nonunitary dissipation of a given system (as described by NHHs), but also on quantum jumps; this is contrary to HEPs which are not affected by them, so in that sense can be considered semiclassical or even classical. The connection between HEPs and LEPs can be demonstrated by postselecting quantum trajectories following the hybrid-Liouvillian formalism [47]. Recent experiments with a single three-level transmon [21, 22] and a single three-level trapped ion [48, 49] have indicated the importance of LEPs by revealing the pivotal significance of quantum jumps in generalizing the applications of classical non-Hermitian systems to open quantum systems. These applications encompass advanced techniques such as precise sensing and control of quantum circuits [21], dynamical manipulation of quantum thermal

machines [50], and specifically the operation of quantum heat engines [49], all exploiting the unique properties of LEPs. The formalism of LEPs is based on the Lindblad master equation, so relies on the standard quantum mechanics, where there is no need for calculating a system-dependent metric [51, 52], thus preventing the apparent violation of the no-go theorems.

Although the complex spectra of Liouvillians have been analyzed previously (see, e.g., Refs. [53, 54, 55, 56, 57] and references therein), interest in Liouvillian singularities, now termed LEPs and Liouvillian diabolical points (LDPs), and their physical significance has only recently been revived by works such as Refs. [58, 59, 46]. Thus, since 2019 there has been a growing theoretical interest stimulated by experimental progress [20, 21, 22, 48, 49] in observing, understanding, and utilizing quantum aspects of Liouvillian singularities. This includes also closely related concepts of Liouvillian diabolical points (i.e., spectral degeneracies, where eigenvalues coalesce, but the associated eigenvectors remain orthogonal) [60, 61], hybrid LEPs (which interpolate between HEPs and LEPs) [47, 21], and higher-order eigenspectrum degeneracies exhibiting hybrid properties of both diabolical and exceptional points [62, 63].

Quantum process tomography (QPT) is a procedure that enables a complete experimental characterization of a quantum black box or, in mathematical terms, the reconstruction of the Liouvillian superoperator characterizing completely the dynamics of an unknown quantum process (see reviews [64, 65, 66] and references therein). Due to the formal equivalence between processes and channels, QPT is often considered a quantum-channel tomography. QPT was introduced in Refs. [67, 68, 69] as a generalization of quantum state tomography (QST) for reconstructing quantum channels via reconstructing quantum output states for various input states. Similarities between QPT and QST include even the use of maximum-likelihood estimation to guarantee that an experimentally reconstructed Liouvillian superoperators (or a density matrix) really describes a physical process (or state) [70, 71]. Anyway, QST and QPT are two related but distinct procedures of quantum engineering: QST aims to reconstruct the quantum state (density matrix) of a system by measuring various observables. This process only tells us about the specific state of a quantum system at a given point. While QPT is used to fully characterize the dynamics or transformation (quantum process) that a system undergoes. It reveals how any input state is mapped to an output state by a quantum channel, gate, or process. These two procedures become equivalent only in a specific scenario when the process itself is simply an identity operation (i.e., it leaves states unchanged), QPT effectively reduces to QST. In this case, the only task left is to determine the state of the system, as there is no transformation occurring. In all other cases, QPT is more complex, as it requires understanding the transformation effects on a full set of basis states, while QST is limited to reconstructing the description of just one state.

First experimental demonstrations of QPT were reported for characterizing two-qubit gates using nuclear-magnetic-resonance (NMR) spectroscopy [72], and single- [73, 74] and two-qubit [75, 76, 77] gates using linear optics and conditional

measurements. A multi-qubit (say n -qubit) QPT can be realized by replicating (n times) a given experimental setup for a single-qubit QPT [74]. This implies that the dimension of a reconstructed Liouvillian superoperator and the complexity of QPT grows exponentially with n . Recent experimental implementations of QPT (and related tomography methods) include: trapped-ion qubit gates [78], superconducting quantum processors [79, 80, 81], photon polarization damping channels [82], and plasmonic metamaterials operating as polarization-dependent loss channels in quantum plasmonics [83], etc. However, to our knowledge, the experimental observation of LEPs of the Liouvillians reconstructed via QPT has not been reported yet.

We analyze and experimentally implement QPT and reveal LEPs using single-, two-, and three-qubit superconducting circuits, shown in Fig. 1, using an IBM quantum (IBMQ) processor [84]. Note that we initially performed simulations on the circuits, both without and with noise, as shown in Figs. 2–4. Only afterward we conducted the actual experiments. Therefore, our main experimental results are presented alongside the simulation results in Figs. 3 and 4.

We argue that various experimental methods used for single-qubit QST [20] and QPT (e.g., [80, 85]) can be modified to induce and reveal LEPs along the lines described here. QPT can enable experimental finding not only LEPs but also quantum diabolical points, which can reveal dissipative phase transitions and a Liouvillian spectral collapse [60, 61]. We note that QST has been applied across LEPs in Refs. [21, 22] (see also Ref. [20]). But to our knowledge QPT has not been applied to reveal LEPs yet. In particular, an LEP-based quantum heat engine was studied experimentally in Refs. [48, 49], but neither QST nor QPT was applied there.

Our work serves primarily as a proof-of-principle study, demonstrating the experimental feasibility and effectiveness of QPT for analyzing quantum system dynamics near LEPs. Another key feature of our paper is that it is the first experimental observation of an LEP in a system that does not exhibit any HEPs, as highlighted in the article’s title, including single-, two-, and three-qubit systems. In our view, this result would hold significant value on its own, even if it had been obtained without the QPT-based approach described here, but rather through established methods used in prior LEP-related experiments. Additionally, we report notable physical phenomena, specifically the direct observation of transitions between non-spiraling and spiraling regimes. These regimes, associated with distinct decay behaviors governed by real and complex Liouvillian eigenvalues, were observed in physical systems (including single-, two-, and three-qubit systems), where LEPs had not previously been experimentally observed. Previous experimental studies were limited to single three-level systems (qutrits).

The paper is organized as follows: In Sec. II, we recall the LEP formalism and describe how to detect LEPs via QPT. In Sec. III, we show the applicability of the method by analyzing a specific prototype model of a lossy driven qubit exhibiting LEPs but not HEPs. By applying completely positive maps with unitary gates, as described in Sec. IV, we implemented the model on IBMQ processors, as reported in Sec. V. The

physical interpretation of transitions observed at LEPs is explained in Sec. VI. Section VII presents a broader discussion of the results, including potential generalizations of the proposed method for non-Markovian systems and the application of complementary approaches for identifying LEPs, followed by concluding remarks. Technical details about the applied superoperator formalism, comparison of various equivalent QPT methods, and our estimations of errors and measurement times are given in Appendices.

2. Liouvillian exceptional points and their detection

Let us consider the dissipative evolution of a quantum system within the Lindblad master equation. We make the standard assumption that the system weakly interacts with a Markovian environment. In the case of the QPT of composite systems (e.g., a qubit and a cavity mode), it is usually also assumed that the interaction between the subsystems (e.g., light and matter) can be either weak or strong, but not ultrastrong, so that each of the subsystems dissipates via a separate dissipative channel, rather than combined channels, which would require applying a generalized master equation [86, 87, 88]. The expected photon output rate in the ultrastrongly coupled light-matter systems is not directly related to the number of photons in a cavity [89]. Thus, a generalized QPT should be applied which, however, is not studied here.

A general-form Lindblad master equation can be expressed via the Liouvillian superoperators \mathcal{L} [90, 91] ($\hbar = 1$) as

$$\frac{\partial}{\partial t} \hat{\rho} = \mathcal{L} \hat{\rho}(t) = -i[\hat{H}, \hat{\rho}(t)] + \sum_{\mu} \mathcal{D}[\hat{\Gamma}_{\mu}] \hat{\rho}(t), \quad (1)$$

acting on the density matrix $\hat{\rho}(t)$ of the system described by a Hermitian Hamiltonian \hat{H} at an evolution moment t . For the clarity of our presentation, the standard matrix representation of superoperators is recalled in Appendix A. The Lindbladian dissipators $\mathcal{D}[\hat{\Gamma}_{\mu}]$ are given by

$$\mathcal{D}[\hat{\Gamma}_{\mu}] \hat{\rho}(t) = \hat{\Gamma}_{\mu} \hat{\rho}(t) \hat{\Gamma}_{\mu}^{\dagger} - \frac{1}{2} [\hat{\Gamma}_{\mu}^{\dagger} \hat{\Gamma}_{\mu} \hat{\rho}(t) + \hat{\rho}(t) \hat{\Gamma}_{\mu}^{\dagger} \hat{\Gamma}_{\mu}], \quad (2)$$

where $\hat{\Gamma}_{\mu}$ are quantum jump operators with a clear interpretation in the quantum-trajectory approach (also referred to as the wave-function Monte Carlo method) [92, 93, 94, 95, 96]. Consequently, one can also introduce an effective NHH,

$$\hat{H}_{\text{eff}} = \hat{H} - \frac{i}{2} \sum_{\mu} \hat{\Gamma}_{\mu}^{\dagger} \hat{\Gamma}_{\mu}, \quad (3)$$

and rewrite Eq. (1) as

$$\mathcal{L} \hat{\rho}(t) = -i [\hat{H}_{\text{eff}} \hat{\rho}(t) - \hat{\rho}(t) \hat{H}_{\text{eff}}^{\dagger}] + \sum_{\mu} \hat{\Gamma}_{\mu} \hat{\rho}(t) \hat{\Gamma}_{\mu}^{\dagger}. \quad (4)$$

This master equation encompasses the terms describing a continuous non-unitary dissipative evolution via \hat{H}_{eff} , and the quantum-jump term. A quantum jump is a sudden stochastic change of the wave-function corresponding to the loss or gain of a system

excitation due to the interaction with the environment, which monitors (“measures”) the system [97, 91]. This quantum-trajectory interpretation of the master equation is physically very intuitive and reveals the importance of effective NHHs, which are used in standard quantum mechanics and are not limited to \mathcal{PT} -symmetric systems. They describe continuous losses of energy, coherence, and quantum information of a system into its environment. Moreover, this master equation interpretation also reveals crucial role of quantum jumps. Their omission can be justified in the semiclassical limit or by postselecting quantum trajectories.

We consider the eigenproblems:

$$\hat{H}_{\text{eff}}|E_n\rangle = E_n|E_n\rangle, \quad (5)$$

$$\mathcal{L}\hat{\rho}_n = \lambda_n\hat{\rho}_n, \quad (6)$$

$$\mathcal{L}^\dagger\hat{\sigma}_n = \lambda_n^*\hat{\sigma}_n, \quad (7)$$

where E_n and $|E_n\rangle$ are the eigenvalues and eigenvectors of the NHH operator; while λ_n , $\hat{\rho}_n$, and $\hat{\sigma}_n$ are the eigenvalues, as well as the right and left eigenmatrices of the Liouvillian superoperator, respectively. With these eigenspectra, HEPs and LEPs can be found. Note that $\hat{\rho}_n$ and $\hat{\sigma}_n$ for a given n are mutually orthogonal. However, different $\hat{\rho}_n$ (as well as $\hat{\sigma}_n$) are not, in general, orthogonal. The real parts of λ_n for any n is non-positive and describes a relaxation rate towards the system’s steady state [90]. By representing the eigenmatrices $\hat{\rho}_n$ and $\hat{\sigma}_n$ as vectors $|\tilde{\rho}_n\rangle$ and $\langle\tilde{\sigma}_n|$, respectively, and treating the Liouvillian superoperator \mathcal{L} as a matrix $\tilde{\mathcal{L}}$, Eqs. (6) and (7) can be rewritten, respectively, as

$$\tilde{\mathcal{L}}|\tilde{\rho}_n\rangle = \lambda_n|\tilde{\rho}_n\rangle \quad \text{and} \quad \langle\tilde{\sigma}_n|\tilde{\mathcal{L}} = \lambda_n\langle\tilde{\sigma}_n|. \quad (8)$$

The LEPs of $\tilde{\mathcal{L}}$ can be calculated by applying the standard superoperator formalism [46]. Such LEPs can be found experimentally via the QPT based on 6×6 projectors, i.e., assuming that the input and output states (or projections) are the eigenstates of all the Pauli operators: $|in_i\rangle, |out_j\rangle \in \{|x_+\rangle, |x_-\rangle, |y_+\rangle, |y_-\rangle, |z_+\rangle, |z_-\rangle\}$, where $|x_\pm\rangle = \frac{1}{\sqrt{2}}(|0\rangle \pm |1\rangle)$, $|y_\pm\rangle = \frac{1}{\sqrt{2}}(|0\rangle \mp i|1\rangle)$, $|z_+\rangle \equiv |0\rangle$, and $|z_-\rangle \equiv |1\rangle$. These projections can be used for the QPT of a transmon qubit, where $|0\rangle$ ($|1\rangle$) corresponds to its ground (excited) state. Thus, for a dissipative and/or amplified process described by the master equation with a Liouvillian \mathcal{L} , one can measure all its elements $L'_{ij} = \langle out_j|\mathcal{L}(\hat{\rho} = |in_i\rangle\langle in_i|)|out_j\rangle$, and, thus, reconstruct the full 6×6 matrix $L = [L'_{ij}]$, which represents \mathcal{L} . We refer to this approach as Method 1. Other approaches can also be applied, including Methods 2 and 3 described in Appendix B. All these methods reveal the same LEPs under perfect measurement conditions as shown in detail in supplementary materials in Supplement 1 and briefly explained in Appendix C.

The dynamics of an open quantum system is governed by Eq. (1). For short evolution steps dt , this corresponds to

$$\hat{\rho}(t+dt) = (\mathcal{L}dt + 1)\hat{\rho}(t) \equiv S\hat{\rho}(t). \quad (9)$$

This short-time evolution of a quantum state $\hat{\rho}(t)$ under the non-Hermitian dynamics, where S is the effective quantum operation, is the subject of QPT. Note that S has

the same spectral decomposition as \mathcal{L} up to an affine transformation for all eigenvalues related to scaling by dt and shifting by 1. Thus, we can study LEPs by performing QPT on S . We choose dt depending on the specific form of \mathcal{L} , being small enough to realize specific dynamics. If the operation S is applied to a system n times, the evolution is effectively described by the master equation for the evolution time ndt .

3. A lossy driven qubit

In our experiment performed on an IBMQ processor [84], we applied QPT to reveal LEPs in a driven lossy single-qubit (spin-1/2) prototype model, which exhibits LEPs but not HEPs [46, 47]. Specifically, the system is described by the Hamiltonian $\hat{H} = (\omega/2)\hat{\sigma}_z$, and decays through three competing channels ($\hat{\sigma}_x$, $\hat{\sigma}_y$, and $\hat{\sigma}_-$), as described by the Liouvillian,

$$\mathcal{L}\hat{\rho}(t) = -i[\hat{H}, \hat{\rho}(t)] + (\gamma_- \mathcal{D}[\hat{\sigma}_-] + \gamma_x \mathcal{D}[\hat{\sigma}_x] + \gamma_y \mathcal{D}[\hat{\sigma}_y])\hat{\rho}(t), \quad (10)$$

where $\hat{\sigma}_{x,y,z}$ are the Pauli matrices, and $\hat{\sigma}_\pm = (\hat{\sigma}_x \mp i\hat{\sigma}_y)/2$ are the qubit raising and lowering operators, respectively. We note that some typos in the corresponding equation in Ref. [46] have been corrected here to ensure that the numerical results can be accurately reproduced. The terms of the master equation describe, respectively: (1) oscillations, (2) erroneous bit flips at a rate γ_- , and (3,4) dissipation with rates γ_x and γ_y along the x - and y -axes of the Bloch sphere, respectively. This dissipative model exhibits a \mathcal{Z}_ϵ symmetry, as it remains invariant under the transformation $\hat{\sigma}_- \rightarrow -\hat{\sigma}_-$ [56, 57]. It is a prototype model that can be applied to various systems beyond the one studied here. For instance, it can describe a spin- $\frac{1}{2}$ particle in a uniform magnetic field along the z -axis, assuming relaxation of the particle along the x - and y -axes, and allowing for spin-flip errors. The oscillations induced by the Hamiltonian, the dissipation occurring along the x and y axes, and the spin flipping induced by $\hat{\sigma}_-$ determine how quickly the system reaches a steady state.

The lack of HEPs is evident due to the diagonal structure of the effective NHH in the standard computational basis, i.e.,

$$\hat{H}_{\text{eff}} = \frac{1}{2}\text{diag}([\omega - i\gamma_x - i\gamma_y - i\gamma_-, -\omega - i\gamma_x - i\gamma_y]), \quad (11)$$

as there is no way to adjust the parameters to make the two eigenvalues equal. Despite this, the Liouvillian still exhibits LEPs. Specifically, one finds the eigenvalues [46]:

$$\begin{aligned} \lambda_0 &= 0, \\ \lambda_{1,2} &= -\frac{\gamma_-}{2} - \gamma_x - \gamma_y \pm \Omega, \\ \lambda_3 &= \gamma_- - 2(\gamma_y + \gamma_x), \end{aligned} \quad (12)$$

together with the corresponding right eigenmatrices:

$$\begin{aligned} \hat{\rho}_0 &\propto \text{diag}([\gamma_x + \gamma_y, \gamma_x + \gamma_y + \gamma_-]), \\ \hat{\rho}_{1,2} &\propto \text{antidiag}([-i\omega \pm \Omega, \gamma_x - \gamma_y]), \\ \hat{\rho}_3 &\propto \text{diag}([-1, 1]), \end{aligned} \quad (13)$$

where $\Omega^2 = \gamma_x^2 + \gamma_y^2 - 2\gamma_x\gamma_y - \omega^2$. See Appendix F for more analytical results. In the case $\gamma_y > \omega$, this Liouvillian exhibits two LEPs at $\gamma_x^\pm \equiv \gamma_y \pm \omega$. We study this configuration experimentally by setting $\gamma_- = 0$ and $\gamma_y = 2\omega$. Figures 2-4 show theoretical eigenvalues $\lambda_{0,1}$ and modified eigenvalues, which are obtained via a more-realistic QPT simulation assuming white noise. Specifically, experimental pure-like states, which are the input states for QPT, are always mixed with some amount of white noise. This undesired effect was included in our refined simulations. These simulated eigenvalues are compared with λ_n^{exp} reconstructed from our single-, two-, and three-qubit experiments.

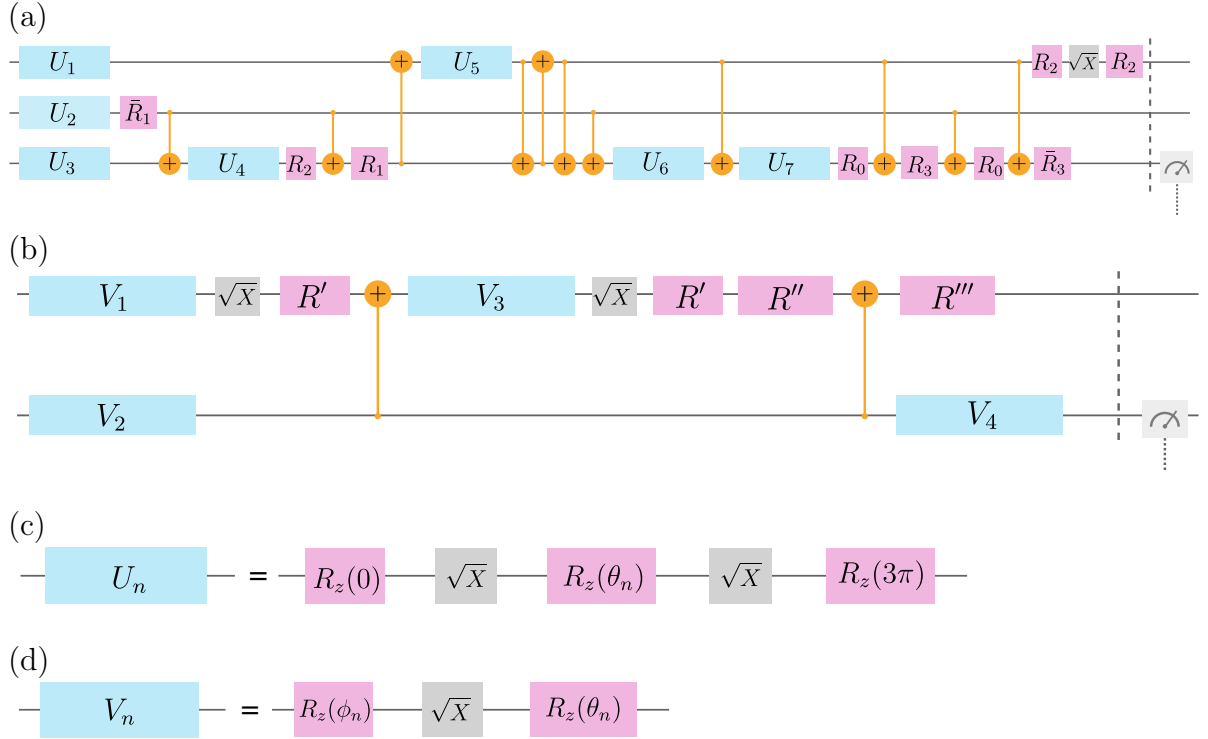


Figure 1. (a) Three-qubit and (b) two-qubit circuits optimized for the Nairobi quantum processor by Qiskit and applied in our experiments. Gates $U_n \equiv U(\theta_n)$ and $V_n \equiv V(\phi_n, \theta_n)$ are implemented by the sequences of basic gates shown in (c) and (d), respectively. We set the following phases for U_n , V_n , $R_n \equiv R_z(\zeta_n)$, and $\bar{R}_n \equiv R_z(-\zeta_n)$: $U_1 = U(5.7153)$, $U_2 = U(4.7788)$, $U_3 = U(5.6341)$, $U_4 = U(2.7850)$, $U_5 = U(3.3259)$, $U_6 = U(3.0600)$, and $U_7 = U(3.4146)$; $V_1 = V(0, 2\pi)$, $V_2 = V(-\pi/2, 0.0332)$, $V_3 = V(0, \pi)$, and $V_4 = V(\pi/2, \pi/2)$; $R_0 = R_z(0)$, $R_1 = R_z(0.0460)$, $R_2 = R_z(\pi/2)$, $R_3 = R_z(1.5248)$, $R' = R_z(3\pi)$, $R'' = R_z(-1.5375)$, and $R''' = R_z(1.6040)$.

4. Implementing completely positive maps with unitary gates

To implement non-Hermitian dynamics using only unitary operations, we purify (coherify) the quantum process by embedding it in a larger Hilbert space, where the joint evolution of the system and its environment is unitary. In particular, starting with the superoperator S , we find its Choi representation $\hat{\chi}$. Depending on the number of

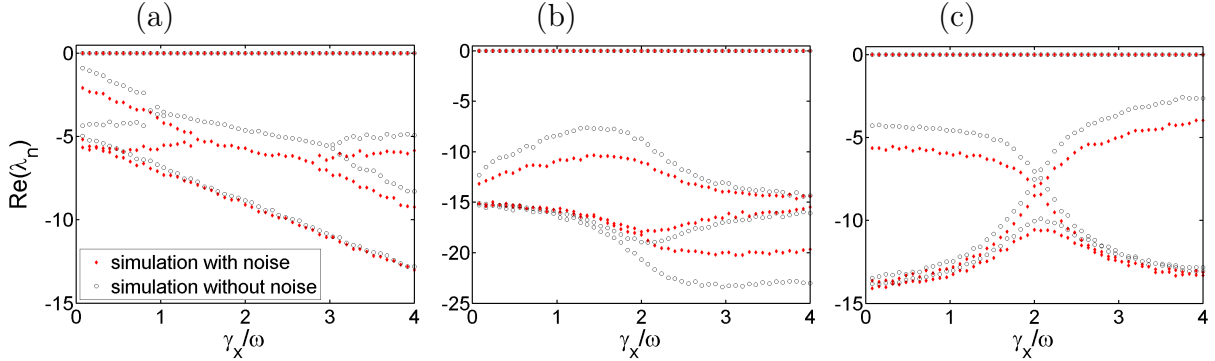


Figure 2. Real parts of the eigenvalues, $\text{Re}(\lambda_n)$, of the Liouvillians simulated for the three-qubit circuit depicted in Fig. 1(a), with measurements conducted on a single qubit: (a) third, (b) second, and (c) first qubit. Simulations were carried out both with (red diamonds) and without (black circles) the inclusion of experimental noise.

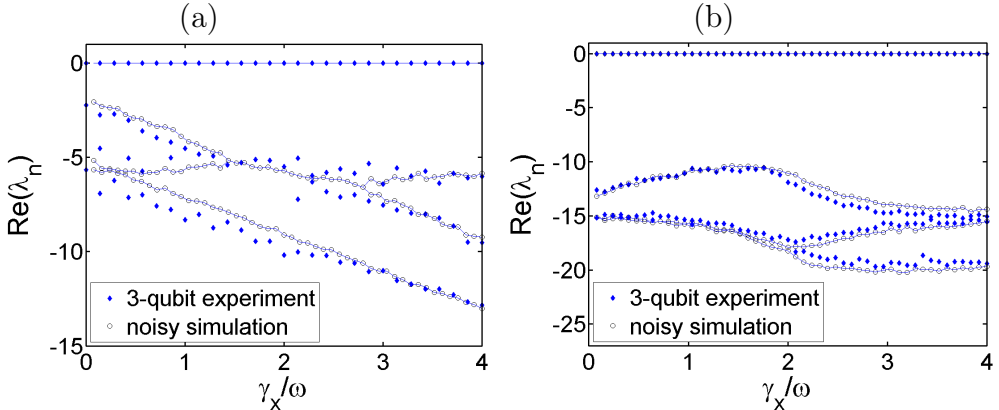


Figure 3. Experimental and simulated real parts of eigenvalues obtained using the 3-qubit circuit, with measurements performed on (a) the third qubit and (b) the second qubit. We note that achieving a close match between the simulated and experimental curves is highly sensitive to the noise mitigation techniques applied in these calculations.

nonzero eigenvalues of the Choi matrix, we choose the dimension of the required ancillary system. This approach to implement completely positive maps is well known (see, e.g., Ref. [98]). As we can implement an arbitrary unitary operation on a programmable quantum computer, we use this approach to demonstrate LEPs experimentally with a noisy intermediate-scale quantum (NISQ) processor.

Completely positive (CP) maps are linear maps that preserve the positivity of density matrices. To express a CP map $\mathcal{E}_\mathcal{H}$ between the Hilbert spaces \mathcal{H} and \mathcal{K} as a unitary operator we can use the Choi-Jamiołkowski isomorphism [99, 100] between the map and operator $\hat{\chi}$. The associated quantum operation can be expressed as

$$\hat{\rho}_{\text{out}} = \text{tr}_\mathcal{H} \left[\hat{\chi} \hat{\rho}_{\text{in}}^T \otimes \hat{1}_\mathcal{K} \right], \quad (14)$$

where the operator, which is isomorphic to the map, reads

$$\hat{\chi} = \mathcal{E}_\mathcal{H} \otimes \mathcal{I}_\mathcal{H} (|\phi\rangle\langle\phi|), \quad (15)$$

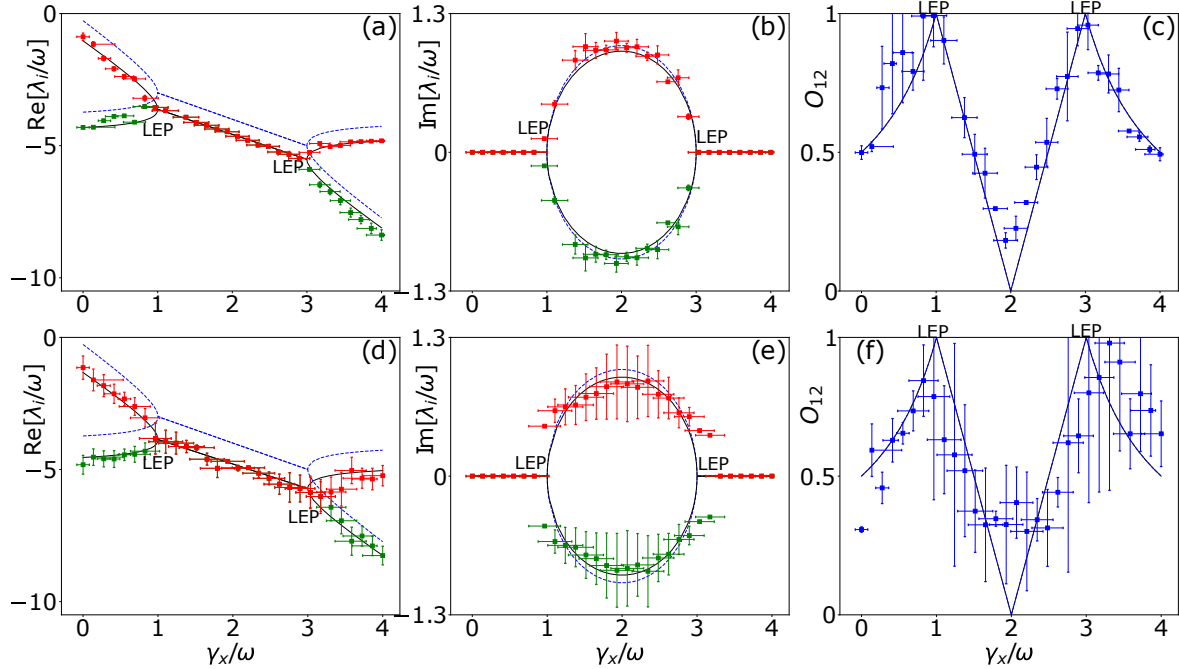


Figure 4. Real (a,d) and imaginary (b,e) parts of the eigenvalues λ_1 and λ_2 of the experimental and theoretical Liouvillians, and the overlaps (c,f), $O_{12} = |\langle \tilde{\sigma}_1 | \tilde{\rho}_2 \rangle|$, of the eigenmatrices $\langle \tilde{\sigma}_1 |$ and $|\tilde{\rho}_2 \rangle$. In the experimental data, λ_1 is indicated by red squares, and λ_2 by green squares when $\lambda_1 \neq \lambda_2$. Experimental results are reconstructed from single-qubit (a,b,c) and two-qubit (d,e,f) measurements performed on an IBMQ processor [84] (squares) and shown together with the corresponding theoretical predictions including white noise (black solid curves) and without it (blue broken curves). Each measurement was carried out with 20,000 shots and $wdt = 1/15$. To enhance plot clarity, the two less relevant real eigenvalues (specifically, $\lambda_0 = 0$ and the smallest eigenvalue λ_3) are omitted here but are displayed in other figures. The results shown in panels (a,b,c) for the single-qubit circuit are clearly less noisy than those in panels (d,e,f) for the two-qubit circuit and are significantly less noisy than the results in Fig. 3(a), which were obtained using the three-qubit circuit. The selected eigenvalues from panels (a, b) and (d, e) are listed explicitly in Tables 1 and 2, respectively.

where $\text{tr}_{\mathcal{K}}[\hat{\chi}] = \hat{\mathbb{1}}_{\mathcal{H}}$, $|\phi\rangle = \sum_{j=1}^{\dim \mathcal{H}} |j\rangle_1 |j\rangle_2$, \mathcal{I} is an identity map, and $\hat{\mathbb{1}}_{\mathcal{H}}$ denotes the identity operator on \mathcal{H} . The corresponding Kraus decomposition reads [98]:

$$\hat{\rho}_{\text{out}} = \mathcal{E}(\hat{\rho}_{\text{in}}) = \sum_l \hat{A}_l \hat{\rho}_{\text{in}} \hat{A}_l^\dagger, \quad (16)$$

where $\sum_l \hat{A}_l^\dagger \hat{A}_l = \hat{\mathbb{1}}_{\mathcal{H}}$, which can be rewritten, by substituting $A_{ki}^{(l)} \equiv \langle k | \hat{A}_l | i \rangle$, as $\sum_{k,l} A_{ki}^{*(l)} A_{kj}^{(l)} = \delta_{ij}$. The number of the \hat{A}_l operators corresponds to the number of nonzero eigenvalues of the $\hat{\chi}$ matrix; $\hat{\chi}$ and \hat{A}_l can be related to each other by the eigenvalues r_l and the eigenstates $|\pi_l\rangle$ of the $\hat{\chi}$ operator: $A_{ki}^{(l)} = \sqrt{r_l} \langle k | \langle i | \pi_l \rangle$, where $|i\rangle \in \mathcal{H}$ and $|k\rangle \in \mathcal{K}$ are the states in the input and output Hilbert spaces, respectively. Finally, we have

$$\hat{\rho}_{\text{out}} = \text{tr}_{\text{env}}[\hat{U} \hat{\rho}_{\text{in}} \otimes (|0\rangle \langle 0|)_{\text{env}} \hat{U}^\dagger], \quad (17)$$

m	γ_x/ω	$\text{Re}\lambda_1$	$\text{Im}\lambda_1$	$\text{Re}\lambda_2$	$\text{Im}\lambda_2$	λ_3	Gap	Remarks
1	0	-0.88	0	-4.31	0	-4.95	0.88	Smallest spectral gap
2	0.83	-3.21	0	-3.52	0	-6.60	3.21	Non-spiraling point nearest LEP 1
3	0.97	-3.55	0.13	-3.55	-0.13	-6.89	3.55	Spiraling point closest to LEP 1
4	2.07	-4.64	1.04	-4.64	-1.04	-9.10	4.64	Largest spiraling
5	2.90	-5.48	0.33	-5.48	-0.33	-10.77	5.48	Spiraling point closest to LEP 2 and largest spectral gap
6	3.03	-5.25	0	-5.90	0	-11.01	5.25	Non-spiraling point nearest LEP 2
7	4.00	-4.82	0	-8.38	0	-12.92	4.82	$\lambda_3^{(7)} = \min_{n,m} \lambda_n^{(m)}$

Table 1. Experimental nonzero eigenvalues $\lambda_n \equiv \lambda_n^{(m)}$ selected from Figs. 4(a) and 4(b) obtained using the single-qubit circuit: Real and imaginary parts of λ_n for chosen values of the damping coefficient γ_x . Both λ_n and γ_x are given in units of ω . The error bars are indicated in the figures. The Liouvillian spectral gap (referred to here simply as the “gap”) is defined as the non-zero eigenvalue with the smallest modulus of its real part. The minimal measured eigenvalue is given by $\lambda_{\min} = \min_{n,m} \lambda_n^{(m)} = \lambda_3^{(7)}$ among all eigenvalues $n = 1, 2, 3$ for the $M = 29$ measured Liouvillians ($m = 1, \dots, M$) plotted in the figures. The trivial zero eigenvalue, $\lambda_0^{(m)} = 0$, is omitted. The terms ‘closest,’ ‘largest,’ and ‘smallest’ specifically refer to the extremal eigenvalues of these experimental Liouvillians.

m	γ_x/ω	$\text{Re}\lambda_1$	$\text{Im}\lambda_1$	$\text{Re}\lambda_2$	$\text{Im}\lambda_2$	λ_3	Gap	Remarks
1	0	-1.14	0	-4.82	0	-5.24	1.14	Smallest spectral gap
2	0.83	-3.04	0	-4.31	0	-6.67	3.04	Non-spiraling point nearest LEP 1
3	0.97	-3.82	0.47	-3.82	-0.47	-7.11	3.82	Spiraling point closest to LEP 1
4	2.48	-5.14	0.89	-5.14	-0.89	-9.66	5.14	Largest spiraling
5	3.31	-6.02	0.38	-6.02	-0.38	-11.40	6.02	Spiraling point closest to LEP 2 and largest spectral gap
6	3.45	-5.85	0	-6.43	0	-11.64	5.85	Non-spiraling point nearest LEP 2
7	0	-5.23	0	-8.26	0	-12.73	5.23	$\lambda_3^{(7)} = \min_{n,m} \lambda_n^{(m)}$

Table 2. Similar to Table 1, but this table presents the experimental eigenvalues selected from Figs. 4(d) and 4(e), which were obtained from $M = 30$ Liouvillians measured on the two-qubit circuit, shown in Fig. 1(b).

where $\hat{U} = \sum_l \hat{A}_l \otimes (|l\rangle\langle 0|)_{\text{env}}$ is the unitary operation decomposable into quantum gates.

For the discussed driven lossy qubit model, the number of the nonzero eigenvalues of the Choi matrix is ≤ 4 . The simplest single-qubit circuit implementing the CP map applies a unitary operation corresponding to $A^{(l)}$ at random with probability r_l , as described by the Kraus representation. When applied repeatedly to the initial quantum state, the resulting final state approximates the time-evolved quantum state of the simulated system. However, this is not a fully quantum simulation of the quantum dynamics, as an external random number generator is required.

The second simplest experiment is embedded in a two-qubit Hilbert space and

utilizes two-qubit unitary operations and a single-qubit environment, $\hat{\rho}_{\text{env}}^{(1)}$, and reads as

$$\hat{\rho}_{\text{out}} \otimes \hat{\rho}_{\text{env}}^{(1)} = \sum_{m=0,2} \hat{\mathcal{A}}_m (\hat{\rho}_{\text{in}} \otimes |0\rangle\langle 0|) \hat{\mathcal{A}}_m^\dagger, \quad (18)$$

where

$$\hat{\mathcal{A}}_m = \sum_{l=0,1} \hat{A}_{l+m} \otimes |l\rangle\langle 0|, \quad (19)$$

which requires using two random two-qubit operations ($m = 0, 2$). Finally, a completely coherent quantum three-qubit experiment requires applying a single unitary operation and a two-qubit environment, as described by Eq. (17).

When working with a programmable quantum computer, we are mostly limited to applying noisy unitary operations and imperfect readout. There are many approaches towards implementing qubits on quantum computers. Here we focus on transmon qubits, which are nowadays commonly used in superconducting quantum processors. These processors are able to implement sets of elementary instructions containing both single- and two-qubit unitary operations. Not every two qubits in a quantum chip are coupled directly. This requires transpiling a given unitary operation into elementary gates according to a coupling map of a given quantum processor. While the fidelities of single- and two-qubit operations are typically high, the gate errors can accumulate to an unacceptable level. If the time required to execute all the gates is comparable to the coherence time T_2 of the used transmons, then the results are largely affected by decoherence. All of these limitations should be taken into account when designing an experiment. It is evident that the experimentally reconstructed dynamics is usually perturbed with respect to the expected one. The effective perturbations in the eigenvalues ($\delta\lambda$) and eigenmatrices ($|\delta\tilde{\rho}_n\rangle$ and $\langle\delta\tilde{\sigma}_n|$) of an experimental Liouvillian $L^{\text{exp}} = L_0 + \delta L$, with the eigenspectrum obtained experimentally, compared to the ideal unperturbed Liouvillian L_0 and its eigenspectrum [denoted with superscript (0)], can be estimated as [101] (see Appendix D for details):

$$\delta\lambda_n \approx \langle\tilde{\sigma}_n^{(0)}|\delta L|\tilde{\rho}_n^{(0)}\rangle, \quad (20)$$

$$|\delta\tilde{\rho}_n\rangle \approx - \sum_{i(i \neq n)} \left(\frac{\langle\tilde{\sigma}_i^{(0)}|\delta L|\tilde{\rho}_n^{(0)}\rangle}{\lambda_i^{(0)} - \lambda_n^{(0)}} \right) |\tilde{\rho}_i^{(0)}\rangle, \quad (21)$$

$$\langle\delta\tilde{\sigma}_n| \approx - \sum_{i(i \neq n)} \left(\frac{\langle\tilde{\sigma}_n^{(0)}|\delta L|\tilde{\rho}_i^{(0)}\rangle}{\lambda_i^{(0)} - \lambda_n^{(0)}} \right) \langle\tilde{\sigma}_i^{(0)}|. \quad (22)$$

The y -axis error bars depicted in Fig. 4 were calculated according to these equations. Thus, based on these estimations, we can select the most noise-robust experimental strategy. Moreover, the uncertainties of γ_x , as plotted in Fig. 4, are estimated in Appendix E.

5. Experiment

Here, we explain how we conducted experiments using the single-, two-, and three-qubit circuits, as illustrated in Fig. 1 for the latter two cases, to demonstrate the LEPs in the

model described by Eq. (10).

The model we experimentally implemented is, in fact, more general than that given by Eq. (10), as we constructed a three-qubit model, which is then reduced to three different single-qubit models. Specifically, by measuring one of the three qubits and tracing out the other two, we could derive the previously studied model, along with two additional models that have not been examined before.

Figure 2 illustrates the real parts of all the eigenvalues of the Liouvillians that describe the dynamics of the three single-qubit dissipative models based on our simulated experiments using the three-qubit circuit shown in Fig. 1(a). Furthermore, we conducted experiments on this circuit, measuring the third qubit to obtain the eigenvalues displayed in Fig. 3(a) and the second qubit for those in Fig. 3(b). These figures present our experimental results alongside their simulations from Fig. 2 for both models.

For the sake of simplicity and clarity, we hereafter focus on the specific cases illustrated in Figs. 2(a), 3(a), and 4, which correspond to the model given by Eq. (10).

In our experiments the system $\hat{\rho}_{\text{in}} \equiv \hat{\rho}(t)$ was prepared in one of the six input states, which are the eigenstates of the three Pauli operators. Then, the evolution under a given map was applied. Finally, we measure $\hat{\rho}_{\text{out}} \equiv \hat{\rho}(t + dt)$ in the x , y , and z bases to reconstruct L (and, consequently, \mathcal{L}). The results of the experiments, conducted on an IBMQ processor (i.e., Nairobi) [84], were plotted in Figs. 3 and 4. The measurements were performed for 30 points with 20,000 shots per experiment, and the evolution step was $\omega dt = 1/15$. Quantum processors are error-sensitive due to their susceptibility to noise and decoherence. To mitigate errors, we used dynamic decoupling. This involves applying a sequence of pulses to each qubit to protect it from ambient noise. The idea behind the method is to repeatedly apply a series of the inversion or refocussing pulses that reverse the effect of noise. These pulses effectively separate the qubit from its environment and can increase the qubit coherence time. This method is conceptually similar to the spin-echo method. Specific examples of our reconstructed Liouvillians including their experimental errors are presented in figures 2-4 in comparison to our theoretical predictions.

Examples of the coupling map and calibration data for the used quantum processor are shown in Fig. 5. Our experiments were implemented on a seven-qubit IBMQ processor (Nairobi) [84] and we used the Qiskit Runtime environment, which provides a controllable error mitigation and suppression to perform our experiment. Note that, we also performed experiments on several other quantum processors (including the Oslo processor) from IBM, which we selected based on their coupling maps. However, the Nairobi processor resulted in the best results compared to our theoretical predictions and the lowest experimental errors.

Specifically, the theoretical and reconstructed process matrices S , at the first LEP in Figs. 4(a) and 4(b), are shown in Fig. 6 obtained for a single-qubit circuit. Analogously, Fig. 7 shows S obtained for the two-qubit circuit [depicted in Fig. 1(b)] for the first LEP in Figs. 4(d) and 1(e). Moreover, in Figs. 4(c) and 4(f), we show the scalar products (overlaps) $O_{12}^{\text{exp}} = |\langle \tilde{\sigma}_1^{\text{exp}} | \tilde{\rho}_2^{\text{exp}} \rangle|$ between the experimental left and right eigenmatrices,

Qubit	$\bar{T}_1(\mu s)$	$\bar{T}_2(\mu s)$	Freq. (GHz)	Anharm. (GHz)	Single-qubit gate error	Basic gates
#5	109 ± 14	76 ± 7	5.18	-0.34	2.98×10^{-4}	I, R_Z, X, \sqrt{X} , CNOT
#4	155 ± 23	20 ± 1	5.29	-0.34	2.68×10^{-4}	
#0	126 ± 15	33 ± 2	5.26	-0.34	2.27×10^{-4}	I, R_Z, X, \sqrt{X}

Table 3. Calibration data of the IBMQ Nairobi superconducting processor used for our experiments with 1 and 2 qubits. Here, R_z is a single-qubit rotation around the z -axis for various angles, while \bar{T}_1 and \bar{T}_2 are, respectively, the relaxation and decoherence times of a given qubit averaged for a few days (i.e., 14–16.04.2023). The CNOT error rate between qubits #4 and #5 is estimated to be 6.5×10^{-3} . Qubit numbers $\#n$ refer to those in Fig. 5. Source: [84].

$\tilde{\sigma}_1^{\text{exp}}$ and $\tilde{\rho}_2^{\text{exp}}$, compared to $O_{12}^{\text{th}} = |\langle \tilde{\sigma}_1^{(0)} | \tilde{\rho}_2^{(0)} \rangle|$ for the ideal theoretical case. It is seen that $\tilde{\sigma}_1^{\text{exp}}$ and $\tilde{\rho}_2^{\text{exp}}$ are practically coalescent (as $O_{12}^{\text{exp}} \approx 1$) near γ_x^\pm confirming the generation of LEPs. We can conclude that the observed bifurcations of the experimental eigenvalues at LEPs for $\gamma_x^\pm = (2 \pm 1)\omega$, and the coalescence of the corresponding eigenmatrices reconstructed for both the single- and two-qubit experiments are in good agreement with our theoretical predictions.

In the single-qubit case, we applied the Qiskit optimization level 1, which enables a single-qubit gate optimization, together the resilience level 1, which enables readout error mitigation. In the two-qubit experiments, we used the optimization level 3, which enables a dynamical decoupling error suppression, together with the resilience level 1. Moreover, we experimentally tested different qubits to find that the best results were obtained for: Qubit #0 in the single-qubit experiment and Qubits #4 and #5 for the two-qubit experiments. See Table 3 for more experimental characteristics of chosen qubits and gates.

In general, our single-qubit experiments are less noisy compared to the two-qubit and, especially, three-qubit experiments. However, at a single point, $\gamma_x/\omega = 1.379$, we observed a sudden jump in both the real and imaginary parts of $\lambda_{1,2}$, with values increasing by three orders of magnitude compared to other measured values in a single-qubit experiment. Consequently, this data point is not visible in Figs. 4(a) and 4(b) as it lies beyond their axis range. In contrast, our two-qubit experiment, along with single-qubit and two-qubit simulations at this point, showed no such singularity. Therefore, this sudden peak is most likely due to a malfunction in the experimental setup.

Finally, we note that our experiments for demonstrating the NHH dynamics are challenging even for simple systems due to highly entangling three-qubit operations $\hat{U}^{(3)} = \sum_l \hat{A}_l \otimes |l\rangle\langle 0|$ implemented by quantum circuits. The results of our three-qubit experiments on IBMQ processors [84] are quite noisy and not shown here. Although our main experimental results, presented in Figs. 3 and 4, are limited to single-, two-, and three-qubit experiments, they show the potential of QPT for revealing and manipulating LEPs.

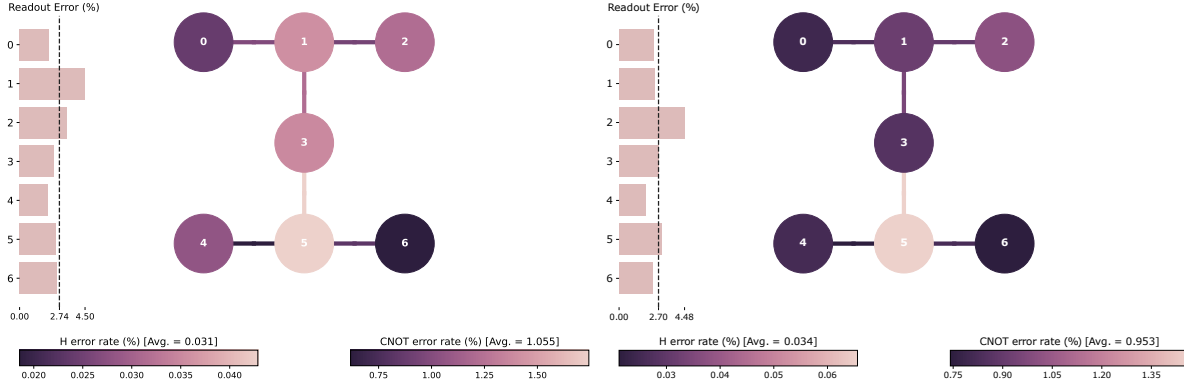


Figure 5. Examples of the calibration data of the seven-qubit IBM quantum processor (i.e., Nairobi) for (a) single- and (b) two-qubit experiments, as completed on 18 and 22 April, 2023, respectively. Source: [84]. Here, H stands for the Hadamard gate.

6. Physical interpretation of transitions at LEPs

Tables 1 and 2 present experimental eigenvalues depicted in Fig. 4, which are essential for interpreting the decay transitions observed at the LEPs. In the ideal version of our model, LEPs should theoretically occur at the γ_x/ω values of 1 and 3. However, in our experiments, these points were shifted. Specifically, for our one-qubit experiments, the first and second LEPs were observed within the ranges (0.83,0.97) and (2.90,3.03), respectively. Similarly, in the two-qubit experiments, the LEPs appeared within the ranges (0.83,0.97) and (3.31,3.45). As indicated in the tables, achieving exact tuning to the LEPs was not possible. For instance, in both experiments, the value $\gamma_x/\omega = 0.97$ already exceeded the first LEP; this suggests that the LEP is shifted from 1 to a slightly smaller value on the γ_x/ω axis, by at least 0.03. Additionally, the second LEP appears shifted from 3 to a slightly smaller value for the one-qubit experiment, whereas in the two-qubit experiment, it is shifted to a much higher value by over 0.31 compared to ideal predictions. Consequently, we were unable to precisely adjust the system to match the experimental LEPs; nonetheless, our measurements for both one- and two-qubit setups are relatively close to these points. For clarity, we refer to LEPs at approximate γ_x/ω values of 1 and 3, understanding that these points are slightly shifted in our experimental configurations.

Before interpreting the observed LEPs and related effects, it is helpful to revisit both the geometric and physical interpretations of four types of system evolutions (paths), each associated with a specific type of a Liouvillian eigenvalue as described in Refs. [55, 56]: Type 1: For $\lambda_n = 0$, the corresponding Liouvillian eigenvectors determine the system's steady state. Type 2: When $\lambda_n < 0$, the system exhibits exponential decay to zero over time. Type 3: If two eigenvalues form a complex-conjugate pair, the system follows a spiraling trajectory as these eigenvalues decay to zero in the infinite-time limit. These three types of eigenvalues are observed in our model. For completeness, we also mention Type 4, which occurs when an eigenvalue is purely imaginary. In this case, the

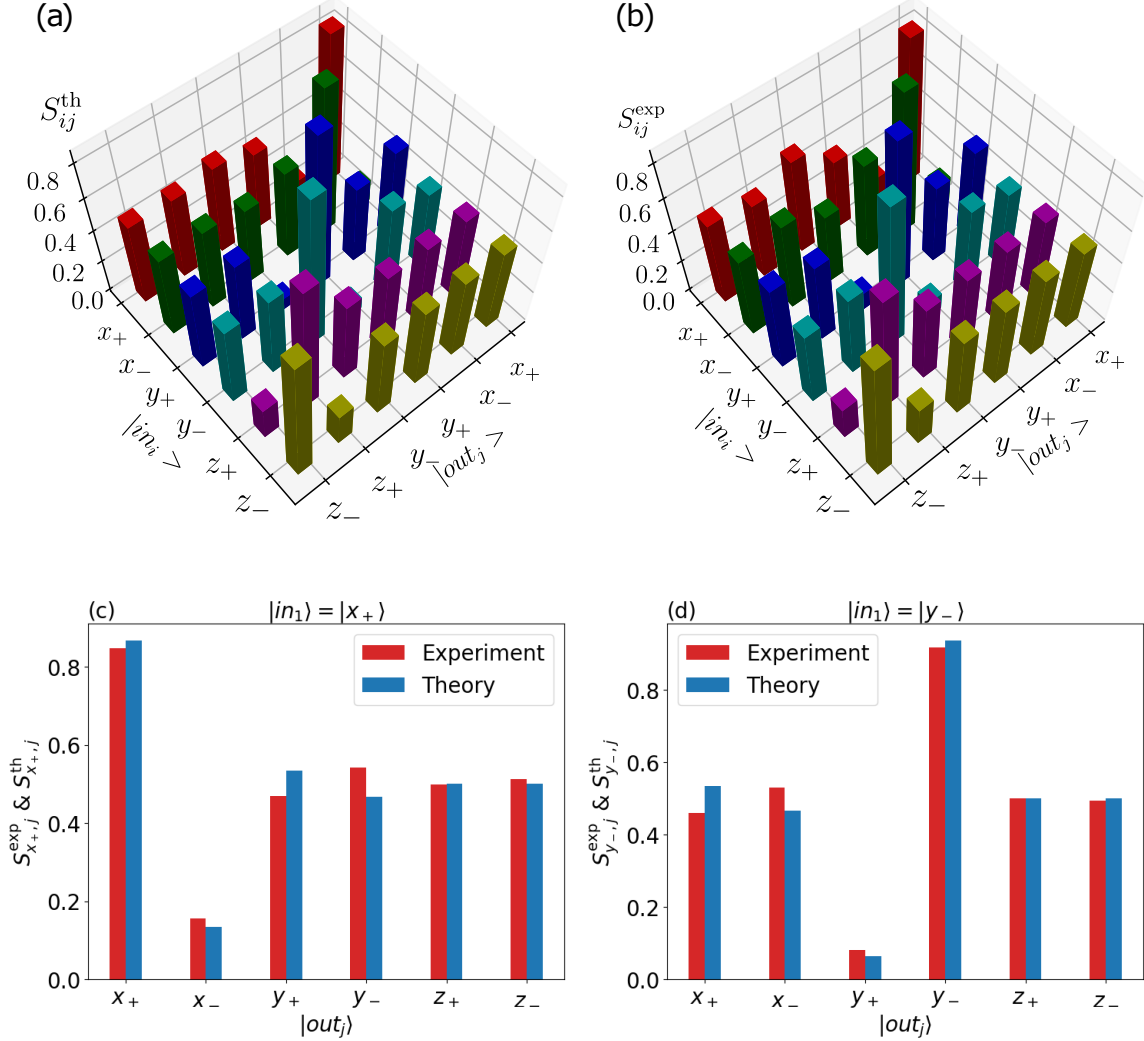


Figure 6. Theoretical (a) and experimental (b) matrix elements $S_{ij} = L'_{ij}dt + 1$, corresponding to the Liouvillian elements L'_{ij} , for our single-qubit experiment performed for $\omega dt = 1/15$ and $\gamma/\omega = 0.96$. These matrices correspond to the first LEP shown in Figs. 4(a) and 4(b). Comparison of the cross-sections of the figures in panels (a) and (b) for chosen input states: $|x_+\rangle$ (c) and $|y_-\rangle$ (d), where the theoretical predictions are represented by blue bars, and the experimental results by red bars.

system exhibits oscillating coherences, following a circular path geometrically. Here, the eigenmatrix associated with such an eigenvalue is preserved in the infinite-time limit. However, Type 4 is not observed in our model. Overall, the general evolution of the system results from the superposition of these distinct types of evolutions.

As shown in Tables 1 and 2, and Figs. 2–4, all four eigenvalues are non-positive for any value of the damping rate γ_x . Specifically, for $\gamma_x/\omega < 1$ and $\gamma_x/\omega > 3$, the eigenvalues are four distinct real values: one zero and three negative. In these regions, the system decay at long times is exponential. In contrast, within the range $\gamma_x/\omega \in (1, 3)$, two of the eigenvalues form a complex-conjugate pair, $\lambda_1 = \lambda_2^*$, accompanied by one zero and one negative eigenvalue, as in the previous cases. Here,

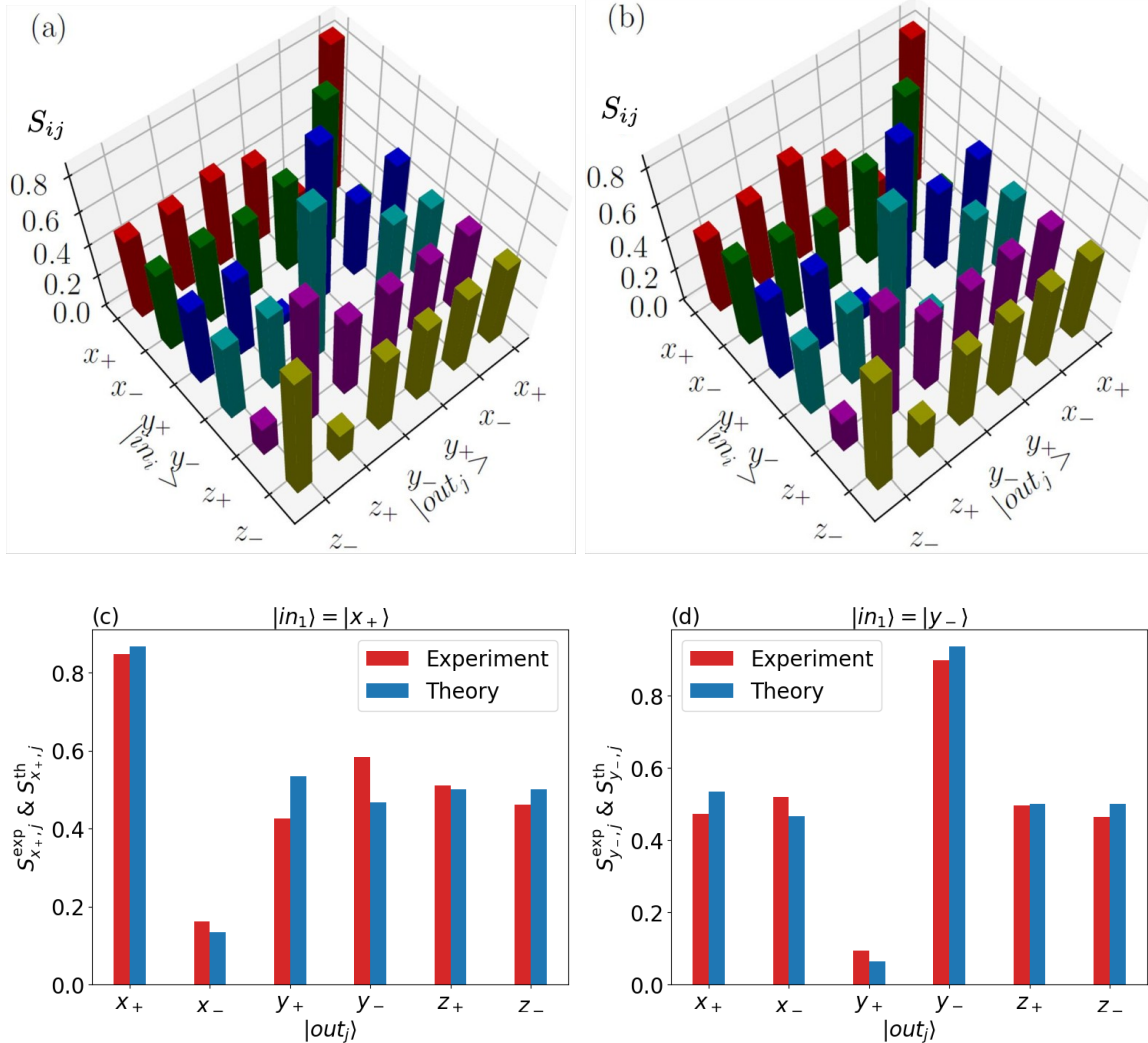


Figure 7. Same as in Fig. 6, but for our two-qubit experiment. These matrices correspond to the first LEP shown in Figs. 4(d) and 4(e).

the decay rate $\text{Re}(\lambda_1) = \text{Re}(\lambda_2)$ is modulated by an oscillatory (or spiraling) term $\text{Im}\lambda_1$. When complex-conjugate pairs with negative real parts are present, the system is in the “spiraling regime,” following a spiral trajectory (superposed with the exponential decay). Otherwise, it is in a “non-spiraling regime,” where decay is purely exponential without oscillations.

At the LEPs, where the Liouvillian is not diagonalizable, the transition between these spiraling and non-spiraling regimes takes place. The tables also show the Liouvillian spectral gap (also known as an asymptotic decay rate), commonly defined as the absolute difference between the real parts of the largest and second-largest eigenvalues of the Liouvillian. Given that $\lambda_0 = 0$ here, the spectral gap is simply $|\text{Re}(\lambda_1)|$, as given in Tables 1 and 2. In Markovian processes (as studied here), the spectral gap correlates with the convergence rate to a steady state, representing the slowest non-zero rate of convergence to the infinite-time state. Therefore, a larger

spectral gap indicates faster system mixing or convergence.

Therefore, the experimental observation of the transitions at the LEPs is not merely a mathematical curiosity; it carries significant physical implications.

7. Discussion and conclusions

We experimentally demonstrated how to engineer and tune a quantum process to approach and detect quantum LEPs via quantum process tomography. We believe it is important to highlight here the following aspects of our experiment in comparison to previous studies:

1. Numerous experimental studies on HEPs have been documented. However, to our knowledge, only four experiments, reported in Refs. [21, 22, 48, 49], focus on LEPs. It is important to emphasize that, unlike HEPs, LEPs account for the effect of quantum jumps [46]. As a result, LEPs represent true quantum phenomena, whereas HEPs are semi-classical, although there are quantum systems in which LEPs and HEPs coincide.
2. For the first time, we experimentally demonstrated a system exhibiting LEPs without HEPs, thus confirming the prediction made in Ref. [46] that such systems exist.
3. Furthermore, to our knowledge, we are the first to report experimental LEPs revealed through QPT. Unlike QST, which reconstructs only quantum states, QPT allows for the complete reconstruction of Liouvillians and their associated LEPs. Previous experimental observations of LEPs in quantum circuits have relied on QST [20, 21, 22].

We note that QST is used to characterize the output state of a quantum processor by measuring the output at various measurement bases assuming that identical states are input to the processor at each run of the QST protocol. QPT on the other hand is used to characterize the map or the transformation that the processor applies to any input state. Here, the processor is probed using different input states and QST is performed at the output of the processor for each of these input states. Thus, QST helps characterize the output state of a processor but does not tell the inner workings of the processor. QPT on the other hand involves QST and is used to understand the inner working of the processor.

4. In previous experimental studies of LEPs [21, 22, 48, 49], a single qutrit was employed to simulate the dissipative evolution of a qubit. In contrast, we use, in particular, two and three qubits on an IBMQ processor to simulate the evolution of a single qubit, leading to a more complex system. We then employed tomographic techniques to reconstruct the experimental Liouvillians and their LEPs using both single- and two-qubit operations.

5. We acknowledge that there are experimental studies on QPT for single superconducting qubits (as discussed below). However, these studies did not reveal any LEPs, as LEPs can only be observed with specifically designed damping and/or amplification channels using precisely tuned parameters. In contrast, our experiment utilized additional qubits to implement the desired damping channels, enabling the

observation of LEPs.

Let us emphasize again that QPT is a well-established method frequently applied to systems like linear-optical setups and trapped ions. However, its applications in circuit QED systems have largely focused on characterizing specific aspects of device performance, such as testing quantum gate fidelities (see, e.g., Refs. [102, 103, 79]). Consequently, QPT has often been replaced by other quantum characterization techniques, including QST, gate set tomography, or randomized benchmarking (see, e.g., Ref. [104] and references therein). Only in a few recent experiments with superconducting qubits, QPT (in generalized forms) has been employed to fully characterize dissipative dynamics [80, 81]. Specifically, in Ref. [80], a refined QPT technique known as Lindblad tomography was developed and used to reconstruct an idling channel, fully characterizing the natural (non-engineered) noise of a superconducting quantum processor. In contrast, our work applies QPT to fully characterize the dynamics of qubits with *specifically engineered* dissipation channels. More importantly, to our knowledge, QPT has not been applied at EPs before. Various studies (see, e.g., Refs. [105, 106, 107, 108, 109, 110, 111, 112] and references therein) showed that noise at EPs can significantly increase, making it unclear, prior to our experiment, whether reliable results could be obtained through QPT at these quantum singularities not only on circuit-QED platform, but on any experimental platform. We have successfully demonstrated that quantum LEPs can indeed be reliably and fully revealed experimentally via QPT.

While QPT enables complete identification and characterization of LEPs, it is not the only approach. QPT can indeed be substituted by alternative approaches such as: (i) topological engineering through encircling an LEP, (ii) Lindblad tomography, or (iii) Heisenberg-Langevin methods. (i) Topological techniques are widely applied to reveal and characterize HEPs in classical physics (see, e.g., Refs. [113, 114, 115] and references therein). Experimental observations of an LEP, which can be considered a form of topological engineering, have been recently reported in Ref. [49], where the enhancement of a quantum Otto heat engine through encircling an LEP was observed. In contrast, (ii) Lindblad tomography, which is a modified QPT method introduced recently in [80], has yet to be employed for LEP identification. Finally, (iii) LEPs can also be fully characterized using the Heisenberg-Langevin equations of motion, as studied theoretically in [62, 116, 117, 118, 119], though these approaches for detecting LEPs in dissipative systems remain experimentally untested.

It is also notable that earlier LEP experimental demonstrations relied not only on reported experiments but on preliminary trials that located these singularities and validated theoretical predictions. In our approach, we reveal LEPs solely using the physical system, independent of a pre-existing theoretical model. This process is illustrated in Figs. 3(b), where we first obtained experimental data and subsequently developed and applied a theoretical simulation shown in Fig. 2(b).

LEPs are distinguished by both degenerate Liouvillian eigenvalues and coalescent eigenmatrices, underscoring the usefulness of Liouvillian tomography in distinguishing

LEPs from Liouvillian diabolical points. Although an LEP can also be identified by measuring topological properties around it [49] (See also topological methods developed for detecting HEPs, such as those discussed in Ref. [120] and references therein), partial QPT is still highly beneficial. It aids in pinpointing a potential LEP, guiding optimal paths to encircle and reveal its topological properties.

Regarding our experiments, the operations for all the experiments are automatically transpiled into a sequence of single- and two-qubit gates, which were physically implemented on a given quantum processor. The physical qubits were selected based on their quality and connectivity, which contribute to the optimal performance of the quantum circuit. To suppress the noise even more, we have explored the state-of-the-art noise-canceling techniques for quantum processors. While we applied experimentally various methods, we found the dynamical decoupling technique to be the most useful. Various QPT methods, which are equivalent under ideal measurement conditions, can be used for revealing LEPs as discussed in Appendix C. However, we observed that the least perturbed Liouvillians for our experimental data were obtained for the QPT method described above (Method 1).

Our experiment and data postprocessing were specifically designed to reconstruct Liouvillian (non-Hermitian) dynamics, not those of an NHH. However, the Hermitian Hamiltonian \hat{H} and the quantum jump operators $\{\hat{L}_\mu\}$, and thus also the corresponding NHH for the studied system could, in principle, be determined using the above-mentioned Lindblad tomography, as demonstrated in a circuit-QED system in Ref. [80]. Lindblad tomography is an adaptation of Liouvillian tomography (i.e., standard QPT), specifically aimed at separately reconstructing the Lindbladian dissipators and Hamiltonian of a given process, rather than directly reconstructing its full Liouvillian. This method relies on a series of pre- and post-pulses to perform rotations needed to reconstruct a channel (or process) at each discrete time step, consistent with standard QPT; and practically the same approach we employed in our experiments. The experimental data, encompassing all combinations of pre- and post-pulses and channel durations, are then processed using a classical optimizer based on maximum likelihood estimation, as detailed in [80]. This postprocessing step in Lindblad tomography differs from standard QPT (i.e. Liouvillian tomography), including the approach we followed, in that we did not apply this type of postprocessing for NHH reconstruction. This is because our primary focus was on demonstrating LEPs, rather than experimentally verifying the absence of HEPs, which we assumed. A strong agreement between the theoretical and experimentally reconstructed Liouvillians, particularly for the single- and two-qubit circuits, also provides indirect validation of our assumption regarding the form of the corresponding NHH and the absence of its HEPs.

We implemented our model using unitary gates, as only unitary operations can be executed on IBMQ. However, the model can also be realized on different platforms, particularly in a linear-optical system. The advantage of such systems is that damping channels can be directly applied to a single qubit, without the need for auxiliary qubits to simulate dissipative evolution. Single- and two-qubit QPT methods can

be readily applied to linear-optical systems, where qubits are encoded in photon polarization. Moreover, controllable damping channels can be implemented through various techniques (see, e.g., Refs. [121, 82] and references therein), making it feasible to realize the current or alternative models exhibiting LEPs in linear-optical systems. This approach could also enable a more precise reconstruction of the Liouvillian, due to significantly lower noise levels of optical systems compared to circuit QED systems.

Regarding experimental feasibility beyond two or three qubits, we emphasize that the IBMQ processors used in our experiments (specifically Nairobi and Oslo) were relatively noisy, which hindered our ability to obtain clear evidence of LEPs with the three-qubit circuits for the studied model. The fidelity achieved was much lower than that of single- and two-qubit circuits, as illustrated by comparing Fig. 3(a) with Figs. 4(a) and 4(d). In contrast, quantum computing platforms based on trapped ions, such as those from IonQ, Honeywell, or Alpine Quantum Technologies (AQT), generally exhibit significantly lower noise levels. Therefore, implementing QPT to reveal and characterize LEPs in larger systems with more qubits appears more feasible on such a platform.

For potential further applications of QPT in identifying LEPs or their generalizations, it is noteworthy that Lin et al. [122] has recently generalized the concept of quantum EPs from Markovian to non-Markovian dynamics. Their approach utilizes exact methods for non-Markovian dynamics, specifically the pseudomode equation of motion and hierarchical equations of motion (see, e.g., Ref. [123] and references therein). Both methods rely on auxiliary degrees of freedom, which can be implemented through additional qubits or by utilizing higher-energy levels in superconducting systems, such as transmons. These auxiliary systems effectively increase the dimensionality of the superoperators being studied, while fundamentally allowing for the application of QPT to identify quantum EPs in non-Markovian systems. The pseudomode approach is particularly analogous to the standard Markovian master equation, possessing a Lindblad-type structure. Thus, as proposed in [122], by defining an extended Liouvillian superoperator, non-Markovian EPs can be characterized by the degeneracies in its complex spectrum. This framework appears well-suited for experimentally generating EPs in non-Markovian systems and revealing them via QPT. Notably, there is no fundamental distinction between applying QPT to the standard master equation and the generalized version based on pseudomodes. The key difference lies in the use of additional auxiliary qubits and/or qudits to simulate the desired non-Markovian dynamics. While there appears to be no fundamental obstacle to applying a modified QPT for revealing LEPs in non-Markovian systems, at least within a few-qubit framework, a more in-depth analysis is necessary to develop the specific details for implementing QPT of experimentally simulated dynamics using IBMQ systems. Moreover, the challenge arises with the increased noise associated with a larger number of qubits. Consequently, implementing such non-Markovian EPs on IBMQ presents significant difficulties as we encounter in the present study. In contrast, utilizing a trapped-ion quantum computer (as mentioned above) could provide a more favorable

platform for realizing these dynamics, given their lower experimental noise.

To highlight potential future studies on LEPs and underscore the importance of this work compared to HEPs, it is worth noting that HEPs have already garnered significant interest for their unique topological and other distinctive properties. This research into HEPs holds value not only for fundamental reasons, such as studying novel types of quantum phase transitions, but also for potential advanced applications, including quantum sensing. However, HEPs rely on a semi-classical dissipation model that omits quantum jumps, potentially leading to fundamental issues, such as the preservation of canonical commutation relations. For small quantum systems, a correct dissipation model (at least without postselection on quantum trajectories) must account for quantum jumps. Consequently, LEPs, as natural extensions of HEPs with proper inclusion of quantum jumps, should be used in place of HEPs. Initial theoretical and experimental results of other groups suggest that encircling an LEP could enhance the efficiency of quantum heat engines [48, 49]. While further research is essential to establish their full potential for improving quantum sensing and the performance of quantum heat engines when encircling LEPs in small quantum systems, we believe such investigations are highly valuable. With future experimental investigations into LEP applications in mind, we have demonstrated that QPT is a practical and effective tool for characterizing, verifying, and validating the dynamics of few-qubit systems near LEPs through precise engineering and control of dissipation channels.

In discussing potential future work, it is worth mentioning Liouvillian diabolical points (LDPs). While LDPs are not the focus of the current work, they can be uniquely revealed by QPT and their occurrence signals intriguing physical phenomena, such as Liouvillian spectral collapse [60] predicted within the Scully-Lamb laser model. Note that HEPs and LEPs for systems described by the Scully-Lamb model have also been predicted [30, 31], and HEPs have even been observed [38, 37].

In summary, since their introduction five years ago, LEPs have garnered increasing interest. The majority of LEP studies remain theoretical, with only five experimental demonstrations to date of LEPs (and only in single qutrits) [20, 21, 22, 48, 49], underscoring the importance of experimental investigations in this field. We believe our work not only presents the first observations of LEPs in one-, two-, and three-qubit systems but also demonstrates the feasibility of process tomography as a universal method for detecting LEPs.

Appendix A. Matrix representation of superoperators

To understand the basic idea of LEPs and their relation to QPT, we recall the matrix formalism of superoperators which applies to Liouvillians. A general matrix \hat{O} can be formally vectorized (or flattened) with a function \mathcal{F} as

$$\hat{O} = \sum_{m,n} O_{mn} |m\rangle\langle n| \rightarrow |\tilde{O}\rangle = \mathcal{F}(\hat{O}) = \sum_{m,n} O_{mn} |m\rangle \otimes |n^*\rangle, \quad (\text{A.1})$$

where $*$ denotes complex conjugate and, for clarity, flattened quantities are henceforth

marked by tilde. Thus, a single-qubit matrix $\hat{\rho}$ can be flattened as

$$\hat{\rho} = \begin{bmatrix} \rho_{00} & \rho_{01} \\ \rho_{10} & \rho_{11} \end{bmatrix} \longrightarrow |\tilde{\rho}\rangle = \mathcal{F}(\hat{\rho}) = [\rho_{00}, \rho_{10}, \rho_{01}, \rho_{11}]^T, \quad (\text{A.2})$$

where T denotes transposition. The inverse function $\mathcal{F}^{-1}(|\tilde{\rho}\rangle)$ gives the standard form of the density matrix $\hat{\rho}$. Arbitrary right-hand-side (RHS) and left-hand-side (LHS) acting superoperators, say $R[\hat{O}_1]$ and $L[\hat{O}_1]$, can be represented by matrices $\tilde{R}[\hat{O}_1]$ and $\tilde{L}[\hat{O}_1]$, defined, respectively, as:

$$\begin{aligned} \tilde{R}[\hat{O}_1]|\tilde{O}\rangle_2 &= (\mathbb{1}_N \otimes \hat{O}_1^T)|\tilde{O}\rangle_2, \\ \tilde{L}[\hat{O}_1]|\tilde{O}\rangle_2 &= (\hat{O}_1 \otimes \mathbb{1}_N)|\tilde{O}\rangle_2, \end{aligned} \quad (\text{A.3})$$

where $\mathbb{1}_N$ is the identity operator of dimension $N = \text{size}(\hat{O}_1)$. By applying this convention, the Liouvillian in the Linblad master equation can be represented as

$$\begin{aligned} \tilde{\mathcal{L}} = & -i(\hat{H} \otimes \mathbb{1}_N - \mathbb{1}_N \otimes \hat{H}^T) \\ & + \sum_n \hat{\Gamma}_n \otimes \hat{\Gamma}_n^* - \frac{1}{2}(\hat{\Gamma}_n^\dagger \hat{\Gamma}_n \otimes \mathbb{1}_N - \mathbb{1}_N \otimes \hat{\Gamma}_n^T \hat{\Gamma}_n^*), \end{aligned} \quad (\text{A.4})$$

or, equivalently,

$$\tilde{\mathcal{L}} = -i(\hat{H}_{\text{eff}} \otimes \mathbb{1}_N - \mathbb{1}_N \otimes \hat{H}_{\text{eff}}^T) + \sum_n \hat{\Gamma}_n \otimes \hat{\Gamma}_n^*, \quad (\text{A.5})$$

in terms of the effective Hamiltonian \hat{H}_{eff} defined in Eq. (3). The last term in Eq. (A.5) represents the effect of quantum jumps on the system evolution. And this effect can be decreased or even completely removed by a proper postselection of quantum trajectories, as described by a hybrid Liouvillian formalism [47].

Appendix B. Equivalent QPT methods for finding exceptional points

LEPs can be calculated via the standard superoperator formalism as described in Ref. [46]. Here we consider three methods of finding LEPs via QPT for a single qubit. The methods are equivalent assuming ideal measurements.

Method 1

From an experimental point of view, it is convenient to determine LEPs via the QPT based on 6×6 projectors, i.e., assuming that the input and output states (projections) are the eigenstates of all the Pauli operators ($i, j = x_+, x_-, y_+, y_-, z_+, z_-$):

$$|\text{in}_i\rangle, |\text{out}_j\rangle \in \{|x_+\rangle, |x_-\rangle, |y_+\rangle, |y_-\rangle, |z_+\rangle, |z_-\rangle\}, \quad (\text{B.1})$$

where $|x_{\pm}\rangle = \frac{1}{\sqrt{2}}(|0\rangle \pm |1\rangle)$, $|y_{\pm}\rangle = \frac{1}{\sqrt{2}}(|0\rangle \mp i|1\rangle)$, $|z_+\rangle \equiv |0\rangle$, and $|z_-\rangle \equiv |1\rangle$. These are arguably the most popular projectors used for QST and QPT of photon polarization qubits, but can also be applied to transmon qubits. Thus, for an amplified-dissipative process, described by the Lindblad master equation with a given Liouvillian \mathcal{L} , one can measure all its elements

$$L'_{ij} = \langle \text{out}_j | \mathcal{L}(\hat{\rho} = |\text{in}_i\rangle\langle \text{in}_i|) | \text{out}_j \rangle, \quad (\text{B.2})$$

and, thus, we can reconstruct the 6×6 transformation matrix L' , which represents \mathcal{L} .

Method 2

LEPs can also be calculated via the QPT for all the Pauli operators ($k = x, y, z$), i.e.,

$$\hat{\sigma}_k = |k_+\rangle\langle k_+| - |k_-\rangle\langle k_-|, \quad (\text{B.3})$$

$$\hat{\sigma}_0 = |z_+\rangle\langle z_+| + |z_-\rangle\langle z_-| = \mathbb{1}, \quad (\text{B.4})$$

which can be obtained via the projections on their eigenstates, given in Eq. (B.1). Thus, by measuring all the elements ($m, n = 0, \dots, 3$):

$$L''_{mn} = \frac{1}{2} \text{tr} [\mathcal{L}(\hat{\sigma}_m) \hat{\sigma}_n], \quad (\text{B.5})$$

where $\hat{\sigma}_1 \equiv \hat{\sigma}_x$, $\hat{\sigma}_2 \equiv \hat{\sigma}_y$, and $\hat{\sigma}_3 \equiv \hat{\sigma}_z$, we can reconstruct the 4×4 Liouvillian matrix L'' representing \mathcal{L} .

Method 3

Formally the simplest approach to find LEPs is via the QPT based on the following 4×4 non-Hermitian input/output projectors ($k, l = 1, \dots, 4$):

$$\hat{\rho}_{\text{in},k}, \hat{\rho}_{\text{out},l} \in \{|0\rangle\langle 0|, |0\rangle\langle 1|, |1\rangle\langle 0|, |1\rangle\langle 1|\}. \quad (\text{B.6})$$

By measuring all the elements

$$L_{kl} = \text{tr} [\mathcal{L}(\hat{\rho}_{\text{in},k})^\dagger \hat{\rho}_{\text{out},l}], \quad (\text{B.7})$$

one can reconstruct the 4×4 transformation matrix L , which represents \mathcal{L} . The method, although formally straightforward, is usually experimentally challenging, and it is not applied here.

Appendix C. Equivalence of Methods 1, 2, and 3 under ideal experimental conditions

Here we briefly demonstrate that all the Liouvillian matrices L , L' , and L'' have the same eigenspectra (up to trivial zero values). It means that the exceptional points corresponding to the nonzero eigenvalues of L , L' , and L'' are of the same order. More details on this equivalence are given in Supplement 1.

The spectral decomposition of L reads $L = UAV$, where A is a diagonal matrix of the singular values of L and the matrices U and V are unitary matrices constructed from the left and right eigenmatrices. It can be verified via direct calculations and using the linearity of the Liouvillians L and L'' that $L = U''L''(U'')^\dagger$, where the respective unitary matrix reads

$$U'' = \frac{1}{\sqrt{2}} \begin{bmatrix} 1 & 0 & 0 & 1 \\ 0 & 1 & -i & 0 \\ 0 & 1 & i & 0 \\ 1 & 0 & 0 & -1 \end{bmatrix}. \quad (\text{C.1})$$

Hence,

$$L'' = [(U'')^\dagger U] A [V U''] = (U'')^\dagger L U'' \quad (\text{C.2})$$

is a spectral decomposition of L'' with the same eigenspectrum as L given by A , but with in general different left and right eigenmatrices given by unitary matrices $(U'')^\dagger U$ and $V(V'')^\dagger$. Similarly, we can write the transformation

$$L'' = U' L' (U')^T, \quad (\text{C.3})$$

where

$$U' = \frac{1}{\sqrt{2}} \begin{bmatrix} 1 & 1 & 0 & 0 & 0 & 0 \\ 0 & 0 & 1 & -1 & 0 & 0 \\ 0 & 0 & 0 & 0 & 1 & -1 \\ 1 & -1 & 0 & 0 & 0 & 0 \end{bmatrix}. \quad (\text{C.4})$$

We note that U^T and $(U')^T$ are the respective pseudoinverse matrices to U and U' , respectively. In Supplement 1, by deriving and applying the unitary version of U' , we demonstrate that L'' and L' have equal ranks. We also demonstrate that L'' and L' have the same nontrivial eigenvalues. Thus, up to the two trivial eigenvalues of L' , the spectra of L , L' , and L'' coincide. This is confirmed by our numerical calculations.

Thus, we have demonstrated that the three methods are formally equivalent, assuming perfect measurements. However, it is important to stress that under realistic measurement conditions, the methods usually lead to slightly different reconstructions of Liouvillians and their LEPs. Analogously, different QST methods, which are formally equivalent under perfect measurement conditions, become inequivalent in realistic situations. Consequently, this leads to varying reconstructions of experimental density matrices (for comparative studies of QST methods based on their condition numbers see Refs. [125, 126, 127, 128]).

Appendix D. Estimation of errors in the eigenspectra of experimental Liouvillians

Here, we estimate, based on the derivation of Ref. [101], how much experimental (or numerical) perturbations can affect the eigenspectra of an Liouvillian superoperator. Let us consider an experimental Liouvillian L^{exp} , with the eigenspectra,

$$\begin{aligned} L^{\text{exp}} |\tilde{\rho}_n^{\text{exp}}\rangle &= \lambda_n^{\text{exp}} |\tilde{\rho}_n^{\text{exp}}\rangle, \\ \langle \tilde{\sigma}_n^{\text{exp}} | L^{\text{exp}} &= \lambda_n^{\text{exp}} \langle \tilde{\sigma}_n^{\text{exp}} |, \end{aligned} \quad (\text{D.1})$$

which slightly differ from the spectra of an ideal Liouvillian L_0 ,

$$\begin{aligned} L_0 |\tilde{\rho}_n^{(0)}\rangle &= \lambda_n^{(0)} |\tilde{\rho}_n^{(0)}\rangle, \\ \langle \tilde{\sigma}_n^{(0)} | L_0 &= \lambda_n^{(0)} \langle \tilde{\sigma}_n^{(0)} |. \end{aligned} \quad (\text{D.2})$$

So, one can write

$$L^{\text{exp}} = L_0 + \delta L, \quad (\text{D.3})$$

assuming that δL is a small perturbation. Note that the completeness relation, $\sum_n |\tilde{\rho}_n^{(0)}\rangle\langle\tilde{\sigma}_n^{(0)}| = \mathbb{1}_4$, and the orthonormality condition, $\langle\tilde{\sigma}_n^{(0)}|\tilde{\rho}_m^{(0)}\rangle = \delta_{nm}$, are satisfied for L_0 , and analogously for the corresponding eigenmatrices of L^{exp} . Thus, if the Liouvillians are diagonalizable (i.e., apart from their LEPs), we have

$$f(L_0) = \sum_i f(\lambda_i^{(0)}) |\tilde{\rho}_i^{(0)}\rangle\langle\tilde{\sigma}_i^{(0)}|, \quad (\text{D.4})$$

$$f(L^{\text{exp}}) = \sum_i f(\lambda_i^{\text{exp}}) |\tilde{\rho}_i^{\text{exp}}\rangle\langle\tilde{\sigma}_i^{\text{exp}}|, \quad (\text{D.5})$$

for any well-behaved functions f of the Liouvillians. Assuming small perturbations in L and in related quantities, we consider their power-series expansions:

$$\begin{aligned} L^{\text{exp}} &= L_0 + \epsilon L_1 + \dots, \\ \lambda_n^{\text{exp}} &= \lambda_n^{(0)} + \epsilon \lambda_n^{(1)} + \dots, \\ |\tilde{\rho}_n^{\text{exp}}\rangle &= |\tilde{\rho}_n^{(0)}\rangle + \epsilon |\tilde{\rho}_n^{(1)}\rangle + \dots, \\ \langle\tilde{\sigma}_n^{\text{exp}}| &= \langle\tilde{\sigma}_n^{(0)}| + \epsilon \langle\tilde{\sigma}_n^{(1)}| + \dots, \end{aligned} \quad (\text{D.6})$$

in some perturbation parameter ϵ . For simplicity, hereafter, we omit all the terms with higher powers of ϵ . So, we can assume that $\delta L \approx \epsilon L_1$. By inserting these expansions into Eq. (D.1), one instantly obtains Eq. (D.2) for all the terms independent of ϵ . Moreover, by collecting all the terms proportional to ϵ in these equations, one obtains:

$$F_n^{(0)} |\tilde{\rho}_n^{(1)}\rangle = -F_n^{(1)} |\tilde{\rho}_n^{(0)}\rangle, \quad (\text{D.7})$$

$$\langle\tilde{\sigma}_n^{(1)}| F_n^{(0)} = -F_n^{(1)} \langle\tilde{\sigma}_n^{(0)}|, \quad (\text{D.8})$$

where $F_n^{(k)} = L_k - \lambda_n^{(k)} \mathbb{1}_4$ for $k = 0, 1$. Multiplying Eq. (D.7) by $\langle\tilde{\sigma}_n|$ from the LHS, one obtains $\lambda_n^{(1)} = \langle\tilde{\sigma}_n^{(0)}| L_1 |\tilde{\rho}_n^{(0)}\rangle$, or, equivalently,

$$\begin{aligned} \delta\lambda &\equiv \lambda_n^{\text{exp}} - \lambda_n^{(0)} \approx \epsilon \lambda_n^{(1)} = \langle\tilde{\sigma}_n^{(0)}| (\epsilon L_1) |\tilde{\rho}_n^{(0)}\rangle \\ &\approx \langle\tilde{\sigma}_n^{(0)}| \delta L |\tilde{\rho}_n^{(0)}\rangle. \end{aligned} \quad (\text{D.9})$$

By applying Eq. (D.4), with $f(L_0) = F_n^{(0)}$, to Eq. (D.7), one obtains

$$|\tilde{\rho}_n^{(1)}\rangle \approx - \sum_{i(i \neq n)} \left(\frac{\langle\tilde{\sigma}_i^{(0)}| L_1 |\tilde{\rho}_n^{(0)}\rangle}{\lambda_i^{(0)} - \lambda_n^{(0)}} \right) |\tilde{\rho}_i^{(0)}\rangle, \quad (\text{D.10})$$

which leads to

$$|\delta\tilde{\rho}_n\rangle \equiv |\tilde{\rho}_n^{\text{exp}}\rangle - |\tilde{\rho}_n^{(0)}\rangle \approx |\delta\tilde{\rho}_n^{(1)}\rangle = \epsilon |\tilde{\rho}_n^{(1)}\rangle. \quad (\text{D.11})$$

Analogously, by using Eq. (D.8), one arrives at

$$\langle\tilde{\sigma}_n^{(1)}| = - \sum_{i(i \neq n)} \left(\frac{\langle\tilde{\sigma}_n^{(0)}| L_1 |\tilde{\rho}_i^{(0)}\rangle}{\lambda_i^{(0)} - \lambda_n^{(0)}} \right) \langle\tilde{\sigma}_i^{(0)}|, \quad (\text{D.12})$$

which leads to

$$\langle\delta\tilde{\sigma}_n| \equiv \langle\delta\tilde{\sigma}_n^{\text{exp}}| - \langle\delta\tilde{\sigma}_n^{(0)}| \approx \langle\delta\tilde{\sigma}_n^{(1)}| \equiv \epsilon \langle\tilde{\sigma}_n^{(1)}|, \quad (\text{D.13})$$

as derived in Ref. [101].

Thus, the error bars O_{12}^{exp} of the scalar products (overlaps) $O_{12}^{\text{exp}} = |\langle \tilde{\sigma}_1^{\text{exp}} | \tilde{\rho}_2^{\text{exp}} \rangle|$ of the experimental eigenmatrices $\langle \tilde{\sigma}_1^{\text{exp}} |$ and $| \tilde{\rho}_2^{\text{exp}} \rangle$, which are shown in Fig. 4, are obtained as

$$\begin{aligned}\delta O_{12}^{\text{exp}} &= |\langle \tilde{\sigma}_1^{\text{exp}} | \tilde{\rho}_2^{\text{exp}} \rangle - \langle \tilde{\sigma}_1^{(0)} | \tilde{\rho}_2^{(0)} \rangle| \\ &= |\langle \delta \tilde{\sigma}_1 | \tilde{\rho}_2^{(0)} \rangle + \langle \tilde{\sigma}_1^{(0)} | \delta \tilde{\rho}_2 \rangle + \langle \delta \tilde{\sigma}_1 | \delta \tilde{\rho}_2 \rangle|.\end{aligned}\quad (\text{D.14})$$

Note that these error bars are affected by the phase factors from the overlaps, which can be arbitrary and depend on the applied diagonalization method. Thus, to avoid this phase dependence, one can redefine $\delta O_{12}^{\text{exp}}$ as

$$\delta \bar{O}_{12}^{\text{exp}} = \left[|\langle \delta \tilde{\sigma}_1 | \tilde{\rho}_2^{(0)} \rangle|^2 + |\langle \tilde{\sigma}_1^{(0)} | \delta \tilde{\rho}_2 \rangle|^2 + |\langle \delta \tilde{\sigma}_1 | \delta \tilde{\rho}_2 \rangle|^2 \right]^{1/2}. \quad (\text{D.15})$$

These error bars are depicted in Fig. D1, and can be compared with those in Fig. 4. Note that the point at $\gamma_x = 0$ in Fig. 4(f) is fully consistent with our theoretical prediction using this redefined error bar, $\delta \bar{S}^{\text{exp}}$, but it is not the case for δS^{exp} .

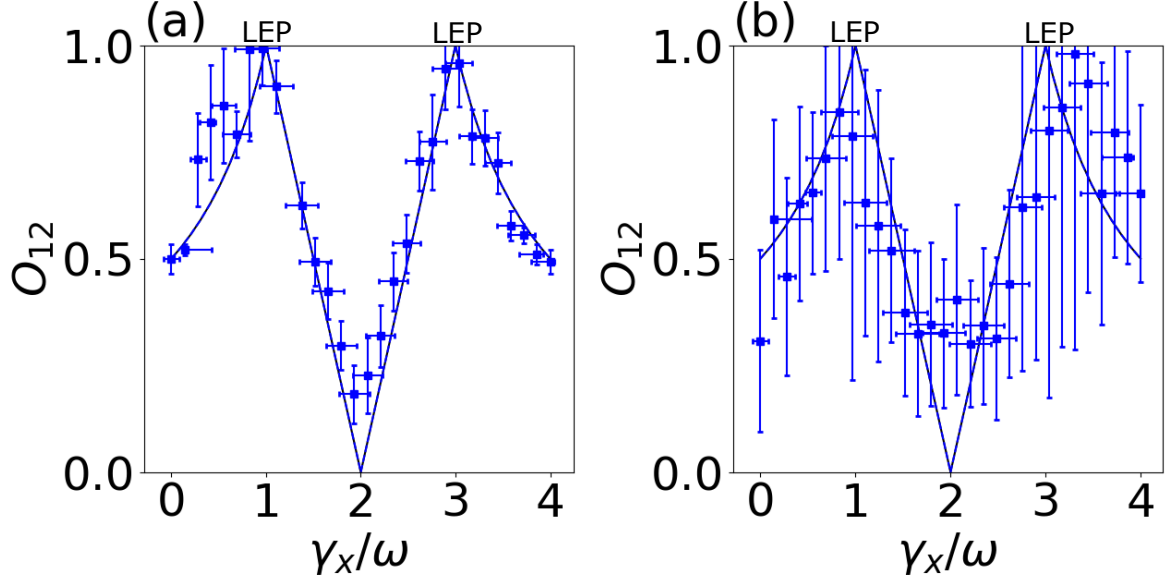


Figure D1. Overlaps $O_{12} = |\langle \tilde{\sigma}_1 | \tilde{\rho}_2 \rangle|$ of the Liouvillian vectorized eigenmatrices $\langle \tilde{\sigma}_1 |$ and $| \tilde{\rho}_2 \rangle$ measured in our single- (a) and two- (b) qubit experiments on an IBMQ processor (blue squares) and compared to the corresponding theoretical predictions including white noise (black curves). Same as Fig. 4, but the error bars $\delta \bar{O}_{12}^{\text{exp}}$ are given here by Eq. (D.15).

Appendix E. Estimation of errors in γ/ω

In our experiments, we intended to prepare quantum circuits to be initially in pure states $|\psi(\gamma)\rangle$, where the dependence on γ is given by the simulated quantum model. However, due to random errors, the prepared states are not exactly the intended pure

states. Instead, we observe that the curves associated with the prepared input states fit the experimental data best if we assume the input state to be

$$\rho = (1 - w)|\psi(\gamma)\rangle\langle\psi(\gamma)| + \frac{w}{d}\mathbb{1}_d, \quad (\text{E.1})$$

where d is the dimension of the Hilbert space and w stands for the level of white noise. On the other hand, there are infinitely many ways to decompose unity or to express the noisy input ρ in a way that is compatible with our observations. In particular, for a given γ , the associated noisy state ρ can be expressed as

$$\rho = \int_{\gamma-\gamma_L}^{\gamma+\gamma_R} p(\gamma + \gamma')|\psi(\gamma + \gamma')\rangle\langle\psi(\gamma + \gamma')|d\gamma', \quad (\text{E.2})$$

where $p(\gamma)$ is a semipositive function defined on $[\gamma - \gamma_L, \gamma + \gamma_R]$, such that ρ is normalized. To simplify the notation, let us set $\gamma = 0$ and $\omega = 1$ in our model. Both expressions for ρ should result in the same fidelity with respect to the target input state $|\psi(\gamma)\rangle$, i.e.,

$$\int_{-\gamma_L}^{\gamma_R} P(\gamma')|\langle\psi(\gamma)|\psi(\gamma')\rangle|^2d\gamma' = 1 - w(1 - 1/d). \quad (\text{E.3})$$

Assume the integrand vanish for $\gamma \geq \gamma_R$ and $\gamma \leq \gamma_L$:

$$p(\gamma')|\langle\psi(\gamma)|\psi(\gamma')\rangle|^2 = 0 \quad \Rightarrow \quad p(\gamma_R) = p(-\gamma_L) = 0. \quad (\text{E.4})$$

Let $p(\gamma)$ reach its maximum at $\gamma = 0$, which can be interpreted as preparing the target state with a maximum likelihood. If we assume that p is a triangular distribution, we arrive at

$$\int_{-\gamma_L}^0 (a_L\gamma' + b)|\langle\psi(\gamma)|\psi(\gamma')\rangle|^2d\gamma' + \int_0^{\gamma_R} (a_R\gamma' + b)|\psi(\gamma')\rangle|^2d\gamma' = 1 - w(1 - 1/d), \quad (\text{E.5})$$

where $a_L = b/\gamma_L$, $a_R = -b/\gamma_R$, and $P(0) = b$. We find b from the normalization condition and $\gamma_{L,R}$ are found numerically from

$$\begin{aligned} & b \int_{-\gamma_L}^{\gamma_R} |\langle\psi(\gamma)|\psi(\gamma')\rangle|^2d\gamma' + \int_{-\gamma_L}^0 a_L|\langle\psi(\gamma)|\psi(\gamma')\rangle|^2\gamma'd\gamma' \\ & + \int_0^{\gamma_R} a_R|\langle\psi(\gamma)|\psi(\gamma')\rangle|^2\gamma'd\gamma' = 1 - w(1 - 1/d). \end{aligned} \quad (\text{E.6})$$

In this way, we estimated the maximum uncertainty in setting γ . In general, we end up with $\gamma_L \neq \gamma_R$, which corresponds to asymmetric uncertainties. We estimate the left and right uncertainties (error bars for γ), respectively, as for two independent triangular distributions to be $P_L\gamma_L/\sqrt{6}$ and $P_R\gamma_R/\sqrt{6}$ [129], where

$$P_L = \int_{-\gamma_L}^0 p(\gamma')d\gamma' \quad \text{and} \quad P_R = \int_0^{\gamma_R} p(\gamma')d\gamma'. \quad (\text{E.7})$$

Appendix F. Analytical formulas for the lossy driven qubit

Here we show analytical results on the QPT of the lossy driven qubit model analyzed in Sec. III.

Case 1: Assuming $\gamma_- = 0$, we have

$$L' = \frac{\omega}{4} \begin{pmatrix} -4 & 4 & -1 & 1 & 0 & 0 \\ 4 & -4 & 1 & -1 & 0 & 0 \\ 1 & -1 & -2x & 2x & 0 & 0 \\ -1 & 1 & 2x & -2x & 0 & 0 \\ 0 & 0 & 0 & 0 & -y_2 & y_2 \\ 0 & 0 & 0 & 0 & y_2 & -y_2 \end{pmatrix}, \quad (\text{F.1})$$

where $x = \gamma/\omega$ and $y_k = 2(x + k)$. The eigenvalues of L' are:

$$\begin{aligned} \lambda'_1 &= -2\omega(2 + x), \\ \lambda'_2 &= -\omega(2 + x - z), \\ \lambda'_3 &= -\omega(2 + x + z), \end{aligned} \quad (\text{F.2})$$

where $z = \sqrt{x^2 - 4x + 3}$, while the other three eigenvalues are zero. The corresponding eigenmatrices are:

$$\begin{aligned} |\tilde{\rho}'_1\rangle &= [0, 0, 0, 0, -1, 1]^T, \\ |\tilde{\rho}'_2\rangle &= [2 - x - z, -2 + x + z, -1, 1, 0, 0]^T, \\ |\tilde{\rho}'_3\rangle &= [2 - x + z, -2 + x - z, -1, 1, 0, 0]^T. \end{aligned} \quad (\text{F.3})$$

Analogously, we find

$$L'' = \omega \begin{pmatrix} 0 & 0 & 0 & 0 \\ 0 & -4 & -1 & 0 \\ 0 & 1 & -2x & 0 \\ 0 & 0 & 0 & -y_2 \end{pmatrix}, \quad (\text{F.4})$$

for which the nonzero eigenvalues of L'' are the same as those of L' : $\lambda'_k = \lambda''_k$ ($k = 1, 2, 3$), but their eigenmatrices:

$$\begin{aligned} |\tilde{\rho}''_1\rangle &= [0, 0, 0, 1]^T, \\ |\tilde{\rho}''_2\rangle &= [0, -2 + x + z, 1, 0]^T, \\ |\tilde{\rho}''_3\rangle &= [0, -2 + x - z, 1, 0]^T, \end{aligned} \quad (\text{F.5})$$

are, in general, different from those of the corresponding ρ'_k .

Case 2: Assuming $\gamma_- = \omega$, we have

$$L' = \frac{\omega}{4} \begin{pmatrix} -9 & 9 & -2 & 2 & 2 & -2 \\ 9 & -9 & 2 & -2 & 2 & -2 \\ 2 & -2 & -4x - 1 & 4x + 1 & 2 & -2 \\ -2 & 2 & 4x + 1 & -4x - 1 & 2 & -2 \\ 0 & 0 & 0 & 0 & -2y_2 & 2y_2 \\ 0 & 0 & 0 & 0 & 2y_3 & -2y_3 \end{pmatrix}, \quad (\text{F.6})$$

having the nonzero eigenvalues equal to:

$$\begin{aligned} \lambda'_1 &= -\omega(2x + 5), \\ \lambda'_2 &= -\frac{\omega}{2}(2x + 5 + 2z), \\ \lambda'_3 &= -\frac{\omega}{2}(2x + 5 - 2z), \end{aligned} \quad (\text{F.7})$$

and the corresponding eigenmatrices:

$$\begin{aligned} |\tilde{\rho}'_1\rangle &= \left[\bar{x}, \bar{x}, \bar{x}, \bar{x}, -\left(\frac{x+3}{x+2}\right), 1 \right]^T, \\ |\tilde{\rho}'_2\rangle &= [2-x-z, -2+x+z, -1, 1, 0, 0]^T, \\ |\tilde{\rho}'_3\rangle &= [2-x+z, -2+x-z, -1, 1, 0, 0]^T, \end{aligned} \quad (\text{F.8})$$

where $\bar{x} = -1/[2(x+2)]$. Analogously, we find

$$L'' = \frac{\omega}{2} \begin{pmatrix} 0 & 0 & -2 & 0 \\ 0 & -4x-1 & 0 & 2 \\ 0 & 0 & -4x-10 & 0 \\ 0 & -2 & 0 & -9 \end{pmatrix}. \quad (\text{F.9})$$

As in Case 1, the *nonzero* eigenvalues of L'' are the same as those of L' : $\lambda'_k = \lambda''_k$ ($k = 1, 2, 3$), but their eigenmatrices are different as given by:

$$\begin{aligned} |\tilde{\rho}''_1\rangle &= \left[\frac{1}{2x+5}, 0, 1, 1 \right]^T, \\ |\tilde{\rho}''_2\rangle &= [0, -2+x+z, 0, 1]^T, \\ |\tilde{\rho}''_3\rangle &= [0, -2+x-z, 0, 1]^T. \end{aligned} \quad (\text{F.10})$$

Appendix G. Measurement times

Here we provide estimates for the total measurement times for the different circuits.

1. For the experiments using the single-qubit circuit: The number of experiments per data point was 72, the number of shots per experiment was 20,000, and the time per shot was 5.7×10^{-6} s. Thus, total number of shots was $N_{\text{total}} = 72 \text{ experiments} \times 20,000 \text{ shots} = 1,440,000 \text{ shots}$ and the total measurement time was $t_{\text{total}} = 1,440,000 \text{ shots} \times 5.7 \times 10^{-6} \text{ s} \approx 8.208 \text{ s}$.

2. For the experiments using the two-qubit circuit [shown in Fig. 1(b)]: The number of experiments per data point was 36, the number of shots per experiment was 20,000, and the time per shot was 6.5×10^{-6} s. Thus, the total number of shots was $N_{\text{total}} = 36 \text{ experiments} \times 20,000 \text{ shots} = 720,000 \text{ shots}$ and the total measurement time was $t_{\text{total}} = 720,000 \text{ shots} \times 6.5 \times 10^{-6} \text{ s} \approx 4.68 \text{ s}$

3. For the experiments using the three-qubit circuit [shown in Fig. 1(a)]: the number of experiments per data point was 18 and we performed 20,000 shots per experiment with the time per shot about 8.9×10^{-6} s. Thus, the total number of shots is given by $N_{\text{total}} = 18 \text{ experiments} \times 20,000 \text{ shots} = 360,000 \text{ shots}$, and the total measurement time was $t_{\text{total}} = 360,000 \text{ shots} \times 8.9 \times 10^{-6} \text{ s} \approx 3.204 \text{ s}$

In summary, the estimated total measurement times are approximately: 8.21s, 4.68s, and 3.20s for our experiments using the single-, two-, and three-qubit circuits, respectively.

The same information can be expressed in the required numbers of the quantum processor cycles. Here, we denote a single quantum processor cycle as τ , instead of

standard dt , to distinguish this time from the time scale of the studied dynamics. In our experiments $\tau = 0.2222$ ns. A single readout takes 2552 cycles, which accumulates to 0.11 s per experiment. Including the measurement time, the execution times of our quantum circuits are: $26 \times 10^3 \tau$, $29 \times 10^3 \tau$, and $40 \times 10^3 \tau$ for the single-, two- and three-qubit experiments, respectively.

Note that an additional approx. 1 – 2 seconds per experiment was required for readout mitigation. This time was allocated for applying dynamical decoupling (similar to the spin-echo method commonly used in NMR) and calibrating signals to account for detector imperfections. This added approximately 72 seconds for the single-qubit experiments, 36 seconds for the two-qubit experiments, and 18 seconds for the three-qubit experiments.

DATA AVAILABILITY

The experimental data and the Qiskit codes used to process the data are available from the corresponding author upon reasonable request.

REFERENCES

- [1] C. M. Bender and S. Boettcher, Real Spectra in Non-Hermitian Hamiltonians having \mathcal{PT} Symmetry, *Phys. Rev. Lett.* **80**, 5243 (1998).
- [2] C. M. Bender, D. C. Brody, and H. F. Jones, Must a Hamiltonian be Hermitian?, *Am. J. Phys.* **71**, 1095 (2003).
- [3] C. M. Bender, Making sense of non-Hermitian Hamiltonians, *Rep. Prog. Phys.* **70**, 947 (2007).
- [4] N. Moiseyev, *Non-Hermitian Quantum Mechanics*, (Cambridge University Press, 2011).
- [5] R. El-Ganainy, K. G. Makris, M. Khajavikhan, Z. H. Musslimani, S. Rotter, and D. N. Christodoulides, Non-Hermitian physics and \mathcal{PT} symmetry, *Nat. Phys.* **14**, 11 (2018).
- [6] A. Guo, G. J. Salamo, D. Duchesne, R. Morandotti, M. Volatier-Ravat, V. Aimez, G. A. Siviloglou, and D. N. Christodoulides, Observation of \mathcal{PT} -symmetry breaking in complex optical potentials, *Phys. Rev. Lett.* **103**, 093902 (2009).
- [7] C. Rüter, K. Makris, R. El-Ganainy, D. N. Christodoulides, M. Segev, and D. Kip, Observation of parity-time symmetry in optics, *Nat. Phys.* **6**, 192 (2010).
- [8] A. Regensburger, C. Bersch, M.-A. Miri, G. Onishchukov, D. N. Christodoulides, and U. Peschel, Parity-time synthetic photonic lattices, *Nature (London)* **488**, 167 (2012).
- [9] J. Schindler, A. Li, M.C. Zheng, F. M. Ellis, and T. Kottos, Experimental study of active LRC circuits with \mathcal{PT} symmetries, *Phys. Rev. A* **84**, 040101(R) (2011).
- [10] H. Benisty *et al.*, Implementation of \mathcal{PT} -symmetric devices using plasmonics: Principle and applications, *Opt. Express* **19**, 18004 (2011).
- [11] M. Kang, F. Liu, and J. Li, Effective spontaneous \mathcal{PT} -symmetry breaking in hybridized metamaterials, *Phys. Rev. A* **87**, 053824 (2013).
- [12] R. Fleury, D. L. Sounas, and A. Alu, Negative refraction and planar focusing based on parity-time symmetric metasurfaces, *Phys. Rev. Lett.* **113**, 023903 (2014).
- [13] Y. Sun, W. Tan, H.-q. Li, J. Li, and H. Chen, Experimental demonstration of a coherent perfect absorber with \mathcal{PT} phase transition, *Phys. Rev. Lett.* **112**, 143903 (2014).
- [14] X. Zhu, H. Ramezani, C. Shi, J. Zhu, and X. Zhang, \mathcal{PT} -symmetric acoustics, *Phys. Rev. X* **4**, 031042 (2014).
- [15] H. Jing, S. K. Özdemir, X.-Y. Lu, J. Zhang, L. Yang, and F. Nori, \mathcal{PT} -symmetric phonon laser, *Phys. Rev. Lett.* **13**, 053604 (2014).
- [16] R. Fleury, D. L. Sounas, and A. Alu, An invisible acoustic sensor based on parity-time symmetry, *Nat. Commun.* **6**, 5905 (2015).

[17] T. Gao *et al.*, Observation of non-Hermitian degeneracies in a chaotic exciton-polariton billiard, *Nature (London)* **526**, 554 (2015).

[18] P. Peng *et al.*, Anti-parity-time symmetry with flying atoms, *Nat. Phys.* **12**, 1139 (2016).

[19] L. Ding, K. Shi, Q. Zhang, D. Shen, X. Zhang, and W. Zhang, Experimental Determination of \mathcal{PT} -Symmetric Exceptional Points in a Single Trapped Ion, *Phys. Rev. Lett.* **126**, 083604 (2021).

[20] M. Naghiloo, M. Abbasi, Y. N. Joglekar, and K. W. Murch, Quantum state tomography across the exceptional point in a single dissipative qubit, *Nat. Phys.* **15**, 1232 (2019).

[21] W. Chen, M. Abbasi, Y. N. Joglekar, and K. W. Murch, Quantum Jumps in the Non-Hermitian Dynamics of a Superconducting Qubit *Phys. Rev. Lett.* **127**, 140504 (2021).

[22] W. Chen, M. Abbasi, B. Ha, S. Erdamar, Y. N. Joglekar, K. W. Murch, Decoherence Induced Exceptional Points in a Dissipative Superconducting Qubit, *Phys. Rev. Lett.* **128**, 110402 (2022).

[23] S. K. Özdemir, S. Rotter, F. Nori, and L. Yang, Parity-time symmetry and exceptional points in photonics, *Nat. Mater.* **18**, 783 (2019).

[24] M. Miri and A. Alù, Exceptional points in optics and photonics, *Science* **363**, eaar7709 (2019).

[25] M. Parto, Y. G. N. Liu, B. Bahari, M. Khajavikhan, and D. N. Christodoulides, Non-Hermitian and topological photonics: Optics at an exceptional point, *Nanophotonics* **10**, 403 (2021).

[26] L. Feng, Z. J. Wong, R.-M. Ma, Y. Wang, and X. Zhang, Single-mode laser by parity-time symmetry breaking, *Science* **346**, 972 (2014).

[27] H. Hodaei, M.-A. Miri, M. Heinrich, D. N. Christodoulides, and M. Khajavikhan, Parity-time-symmetric microring lasers, *Science* **346**, 975 (2014).

[28] B. Peng, S. K. Özdemir, S. Rotter, H. Yilmaz, M. Lierter, F. Monifi, C. M. Bender, F. Nori, and L. Yang, Loss-induced suppression and revival of lasing, *Science* **346**, 328 (2014).

[29] M. Brandstetter, M. Lierter, C. Deutsch, P. Klang, J. Schoberl, H. E. Tureci, G. Strasser, K. Unterrainer, and S. Rotter, Reversing the pump dependence of a laser at an exceptional point, *Nat. Commun.* **5**, 4034 (2014).

[30] I. I. Arkhipov, A. Miranowicz, O. Di Stefano, R. Stassi, S. Savasta, F. Nori, and S. K. Özdemir, Scully-Lamb quantum laser model for parity-time-symmetric whispering-gallery microcavities: Gain saturation effects and non-reciprocity, *Phys. Rev. A* **99**, 053806 (2019).

[31] I. I. Arkhipov, A. Miranowicz, F. Minganti, and F. Nori, Quantum and semiclassical exceptional points of a linear system of coupled cavities with losses and gain within the Scully-Lamb laser theory, *Phys. Rev. A* **101**, 013812 (2020).

[32] A. Pick, B. Zhen, O. D. Miller, C. W. Hsu, F. Hernandez, A. W. Rodriguez, M. Soljacic, and S. G. Johnson, General theory of spontaneous emission near exceptional points, *Opt. Express* **25**, 12325 (2017).

[33] W. D. Heiss and H. L. Harney, The chirality of exceptional points, *Eur. Phys. J. D* **17**, 149 (2001).

[34] C. Dembowski, B. Dietz, H.-D. Gräf, H. L. Harney, A. Heine, W. D. Heiss, and A. Richter, Observation of a Chiral State in a Microwave Cavity, *Phys. Rev. Lett.* **90**, 034101 (2003).

[35] W. R. Sweeney, C.W. Hsu, S. Rotter, and A. D. Stone, Perfectly Absorbing Exceptional Points and Chiral Absorbers, *Phys. Rev. Lett.* **122**, 093901 (2019).

[36] Z. Lin, H. Ramezani, T. Eichelkraut, T. Kottos, H. Cao, and D. N. Christodoulides, Unidirectional Invisibility Induced by \mathcal{PT} -Symmetric Periodic Structures, *Phys. Rev. Lett.* **106**, 213901 (2011).

[37] L. Chang, X. Jiang, S. Hua, C. Yang, J. Wen, L. Jiang, G. Li, G. Wang, and M. Xiao, Parity-time symmetry and variable optical isolation in active-passive-coupled microresonators, *Nat. Photon.* **8**, 524 (2014).

[38] B. Peng, S. K. Özdemir, F. Lei, F. Monifi, M. Gianfreda, G. L. Long, S. Fan, F. Nori, C. M. Bender, and L. Yang, Parity-time-symmetric whispering-gallery microcavities, *Nat. Phys.* **10**, 394 (2014).

[39] J. Peřina Jr., A. Lukš, J. K. Kalaga, W. Leoński, and A. Miranowicz, Nonclassical light at exceptional points of a quantum \mathcal{PT} -symmetric two-mode system, *Phys. Rev. A* **100**, 053820 (2019).

[40] R. Huang, S. K. Özdemir, J. Q. Liao, F. Minganti, L.-M. Kuang, F. Nori, and H. Jing, Exceptional

Photon Blockade: Engineering Photon Blockade with Chiral Exceptional Points, *Laser Photon. Rev.* **16**, 2100430 (2022).

[41] H. Hodaei, U. H. Absar, S. Wittek, H. Garcia-Gracia, R. El-Ganainy, D. N. Christodoulides, and M. Khajavikhan, Enhanced sensitivity at higher-order exceptional points, *Nature (London)* **548**, 187 (2017).

[42] H. Jing, S. K. Özdemir, H. Lü, and F. Nori, High-order exceptional points in optomechanics, *Sci. Rep.* **7**, 3386 (2017).

[43] I. I. Arkhipov, A. Miranowicz, F. Minganti, and F. Nori, Liouvillian exceptional points of any order in dissipative linear bosonic systems: Coherence functions and switching between \mathcal{PT} and anti- \mathcal{PT} symmetries, *Phys. Rev. A* **102**, 033715 (2020).

[44] I. I. Arkhipov, F. Minganti, A. Miranowicz, and F. Nori, Generating high-order quantum exceptional points, *Phys. Rev. A* **104**, 012205 (2021).

[45] E. Lange, A. Kowalewska-Kudłaszyk, G. Chimczak, K. Bartkiewicz, Rotation-time symmetry in bosonic systems and the existence of exceptional points in the absence of \mathcal{PT} -symmetry, *Sc. Rep.* **10**, 19906 (2020).

[46] F. Minganti, A. Miranowicz, R. W. Chhajlany, and F. Nori, Quantum exceptional points of non-Hermitian Hamiltonians and Liouvillians: The effects of quantum jumps, *Phys. Rev. A* **100**, 062131 (2019).

[47] F. Minganti, A. Miranowicz, R. W. Chhajlany, I. I. Arkhipov, and F. Nori, Hybrid-Liouvillian formalism connecting exceptional points of non-Hermitian Hamiltonians and Liouvillians via postselection of quantum trajectories, *Phys. Rev. A* **101**, 062112 (2020).

[48] J.-W. Zhang *et al.*, Dynamical control of quantum heat engines using exceptional points, *Nat. Commun.* **13**, 6225 (2022).

[49] J.-T. Bu *et al.*, Enhancement of Quantum Heat Engine by Encircling a Liouvillian Exceptional Point, *Phys. Rev. Lett.* **130**, 110402 (2023).

[50] S. Khandelwal, N. Brunner, and G. Haack, Signatures of Liouvillian exceptional points in a quantum thermal machine, *PRX Quantum* **2**, 040346 (2021).

[51] C.-Y. Ju, A. Miranowicz, G.-Y. Chen, F. Nori, Non-Hermitian Hamiltonians and no-go theorems in quantum information, *Phys. Rev. A* **100**, 062118 (2019).

[52] C.-Y. Ju, A. Miranowicz, F. Minganti, C.-Ts. Chan, G.-Y. Chen, and F. Nori, Flattening the Curve with Einstein's Quantum Elevator: Hermitization of Non-Hermitian Hamiltonians via the Vielbein Formalism, *Phys. Rev. Res.* **4**, 023070 (2022).

[53] A. Rivas and S. F. Huelga, *Open Quantum Systems: An Introduction*, SpringerBriefs in Physics (Springer Berlin Heidelberg, 2011).

[54] B. Baumgartner, H. Narnhofer, W. Thirring, Analysis of quantum semigroups with GKS-Lindblad generators I. Simple generators, *J. Phys. A: Math. Theor.* **41**, 065201 (2008).

[55] B. Baumgartner and H. Narnhofer, Analysis of quantum semigroups with GKS-Lindblad generators: II. General, *J. Phys. A: Math. Theor.* **41**, 395303 (2008).

[56] V. V. Albert and L. Jiang, Symmetries and conserved quantities in Lindblad master equations, *Phys. Rev. A* **89**, 022118 (2014).

[57] F. Minganti, A. Biella, N. Bartolo, and C. Ciuti, Spectral theory of Liouvillians for dissipative phase transitions, *Phys. Rev. A* **98**, 042118 (2018).

[58] T. Mathisen and J. Larson, Liouvillian of the Open STIRAP Problem, *Entropy* **20** (1), 20 (2018).

[59] N. Hatano, Exceptional points of the Lindblad operator of a two-level system, *Mol. Phys.* **117** (15-16), 2121-2127 (2019).

[60] F. Minganti, I. I. Arkhipov, A. Miranowicz, and F. Nori, Liouvillian spectral collapse in the Scully-Lamb laser model, *Phys. Rev. Res.* **3**, 043197 (2021).

[61] F. Minganti, I. I. Arkhipov, A. Miranowicz, and F. Nori, Continuous Dissipative Phase Transitions with or without Symmetry Breaking, *New J. Phys.* **23**, 122001 (2021).

[62] J. Peřina, Jr., A. Miranowicz, G. Chimczak, and A. Kowalewska-Kudłaszyk, Quantum Liouvillian exceptional and diabolical points for bosonic fields with quadratic Hamiltonians: The Heisenberg-

Langevin equation approach, *Quantum* **6**, 883 (2022).

[63] I. I. Arkhipov, A. Miranowicz, F. Minganti, S. K. Özdemir, and F. Nori, Dynamically encircling an exceptional curve by crossing diabolic points: A programmable multimode switch, *Nat. Comm.* **14**, 2076 (2023).

[64] M. A. Nielsen and I. L. Chuang, *Quantum Computation and Quantum Information* (Cambridge University Press, Cambridge, UK, 2000).

[65] G. M. D'Ariano, M. G. A. Paris, and M. F. Sacchi, Quantum Tomography, *Adv. Imaging Electron Phys.* **128**, 205 (2003).

[66] M. Mohseni, A. T. Rezakhani, and D. A. Lidar, Quantum Process Tomography: Resource Analysis of Different Strategies, *Phys. Rev. A* **77**, 032322 (2008).

[67] I.L. Chuang and M.A. Nielsen, Prescription for experimental determination of the dynamics of a quantum black box, *J. Mod. Opt.* **44**, 2455 (1997).

[68] J. Poyatos, J. Cirac, and P. Zoller, Complete characterization of a quantum process: The two-bit quantum gate, *Phys. Rev. Lett.* **78**, 390 (1997).

[69] G. M. D'Ariano and L. Maccone, Measuring Quantum Optical Hamiltonians, *Phys. Rev. Lett.* **80**, 5465 (1998).

[70] *Quantum State Estimation*, edited by M.G.A. Paris and J. Řeháček (Springer, Berlin, 2004), Vol. 649.

[71] J. Fiurášek and Z. Hradil, Maximum-likelihood estimation of quantum processes, *Phys. Rev. A* **63**, 020101(R) (2001).

[72] A. M. Childs, I.L. Chuang, and D.W. Leung, Realization of quantum process tomography in NMR, *Phys. Rev. A* **64**, 012314 (2001).

[73] J. B. Altepeter *et al.*, Ancilla-Assisted Quantum Process Tomography, *Phys. Rev. Lett.* **90**, 193601 (2003).

[74] F. De Martini, A. Mazzei, M. Ricci, and G. M. D'Ariano, Exploiting quantum parallelism of entanglement for a complete experimental quantum characterization of a single-qubit device, *Phys. Rev. A* **67**, 062307 (2003).

[75] J. L. O'Brien, G. J. Pryde, A. G. White, T. C. Ralph, and D. Branning, Demonstration of an all-optical quantum controlled-NOT gate, *Nature (London)* **426**, 264 (2003).

[76] M.W. Mitchell, C.W. Ellenor, S. Schneider, and A.M. Steinberg, Diagnosis, Prescription, and Prognosis of a Bell-State Filter by Quantum Process Tomography, *Phys. Rev. Lett.* **91**, 120402 (2003).

[77] J. L. O'Brien *et al.*, Quantum process tomography of a controlled-not gate, *Phys. Rev. Lett.* **93**, 080502 (2004).

[78] E. B. Av, Y. Shapira, N. Akerman, and R. Ozeri, Direct reconstruction of the quantum-master-equation dynamics of a trapped-ion qubit, *Phys. Rev. A* **101**, 062305 (2020).

[79] A. Shukla, M. Sisodia, and A. Pathak, Complete characterization of the directly implementable quantum gates used in the IBM quantum processors, *Phys. Lett. A* **384**, 126387 (2020).

[80] G. O. Samach *et al.*, Lindblad Tomography of a Superconducting Quantum Processor, *Phys. Rev. App.* **18**, 064056 (2022).

[81] Q. Pears Stefano, I. Perito, and L. Rebón, Selective and Efficient Quantum Process Tomography for Non-Trace-Preserving Maps: Implementation with a Superconducting Quantum Processor, *Phys. Rev. Applied* **19**, 044065 (2023).

[82] H.-Y. Ku, J. Kadlec, A. Černoch, W. Zhou, K. Lemr, N. Lambert, A. Miranowicz, S.-L. Chen, F. Nori, and Y.-N. Chen, Detecting quantum non-breaking channels without entanglement, *PRX Quantum* **3**, 020338 (2022).

[83] M. Asano, M. Bechu, M. Tame, S. K. Özdemir, R. Ikuta, D. O. Guney, T. Yamamoto, M. Wegener, and N. Imoto, Distillation of photon entanglement using a plasmonic metamaterial, *Sci. Rep.* **5**, 18313 (2015).

[84] IBM Quantum Platform, <https://quantum.ibm.com/> (2024).

[85] M. Howard, J. Twamley, C. Wittmann, T. Gaebel, F. Jelezko, and J. Wrachtrup, Quantum process

tomography and Linblad estimation of a solid-state qubit, *New J. Phys.* **8**, 33 (2006).

[86] F. Beaudoin, J. M. Gambetta, and A. Blais, Dissipation and ultrastrong coupling in circuit QED, *Phys. Rev. A* **84**, 043832 (2011).

[87] A. Settineri, V. Macri, A. Ridolfo, O. Di Stefano, A. F. Kockum, F. Nori, and S. Savasta, Dissipation and thermal noise in hybrid quantum systems in the ultrastrong-coupling regime, *Phys. Rev. A* **98**, 053834 (2018).

[88] A. Mercurio, S. Abo, F. Mauceri, E. Russo, V. Macri, A. Miranowicz, S. Savasta, and O. Di Stefano, Pure Dephasing of Light-Matter Systems in the Ultrastrong and Deep-Strong Coupling Regimes, *Phys. Rev. Lett.* **130**, 123601 (2023).

[89] A. F. Kockum, A. Miranowicz, S. De Liberato, S. Savasta, and F. Nori, Ultrastrong coupling between light and matter, *Nat. Rev. Phys.* **1**, 19 (2019).

[90] H. Breuer and F. Petruccione, *The Theory of Open Quantum Systems* (Oxford University Press, Oxford, 2007).

[91] S. Haroche and J. M. Raimond, *Exploring the Quantum: Atoms, Cavities, and Photons* (Oxford University Press, Oxford, 2006).

[92] J. Dalibard, Y. Castin, and K. Mølmer, Wave-Function Approach to Dissipative Processes in Quantum Optics, *Phys. Rev. Lett.* **68**, 580 (1992).

[93] H. J. Carmichael, Quantum Trajectory Theory for Cascaded Open Systems, *Phys. Rev. Lett.* **70**, 2273 (1993).

[94] K. Mølmer, Y. Castin, and J. Dalibard, Monte Carlo wavefunction method in quantum optics, *J. Opt. Soc. Am. B* **10**, 524 (1993).

[95] M. B. Plenio and P. L. Knight, The quantum-jump approach to dissipative dynamics in quantum optics, *Rev. Mod. Phys.* **70**, 101 (1998).

[96] A. J. Daley, Quantum trajectories and open many-body quantum systems, *Adv. Phys.* **63**, 77 (2014).

[97] H. J. Carmichael, *Statistical Methods in Quantum Optics 1: Master Equations and Fokker-Planck Equations* (Springer, Berlin, 1999).

[98] J. Fiurášek, Extremal equation for optimal completely positive maps, *Phys. Rev. A* **64**, 062310 (2001).

[99] A. Jamiołkowski, Linear transformations which preserve trace and positive semidefiniteness of operators, *Rep. Math. Phys.* **3**, 275 (1972).

[100] M.-D. Choi, Completely positive linear maps on complex matrices, *Lin. Alg. Appl.* **10**, 85 (1975).

[101] D. F. V. James, P. G. Kwiat, W. J. Munro, and A. G. White, Measurement of qubits, *Phys. Rev. A* **64**, 052312 (2001).

[102] R. C. Bialczak, M. Ansmann, M. Hofheinz, E. Lucero, M. Neeley, A. D. O’Connell, D. Sank, H. Wang, J. Wenner, M. Steffen, A. N. Cleland, and J. M. Martinis, Quantum process tomography of a universal entangling gate implemented with Josephson phase qubits, *Nat. Phys.* **6**, 409 (2010).

[103] A. V. Rodionov, A. Veitia, R. Barends, J. Kelly, D. Sank, J. Wenner, J. M. Martinis, R. L. Kosut, and A. N. Korotkov, Compressed sensing quantum process tomography for superconducting quantum gates, *Phys. Rev. B* **90**, 144504 (2014).

[104] J. Eisert, D. Hangleiter, N. Walk, I. Roth, D. Markham, R. Parekh, U. Chabaud, and E. Kashefi, Quantum certification and benchmarking, *Nat. Rev. Phys.* **2**, 382 (2020).

[105] W. Langbein, No exceptional precision of exceptional point sensors, *Phys. Rev. A* **98**, 023805 (2018).

[106] N. A. Mortensen, P. A. D. Goncalves, M. Khajavikhan, D. N. Christodoulides, C. Tserkezis, and C. Wolff, Fluctuations and noise-limited sensing near the exceptional point of parity-time-symmetric resonator systems, *Optica* **5**, 1342 (2018).

[107] H.-K. Lau and A. A. Clerk, Fundamental limits and nonreciprocal approaches in non-Hermitian quantum sensing, *Nature Communications* **9**, 4320 (2018).

[108] C. Wolff, C. Tserkezis, and N. A. Mortensen, On the time evolution at a fluctuating exceptional point, *Nanophotonics* **8**, 1319 (2019).

- [109] M. Zhang, W. Sweeney, C. W. Hsu, L. Yang, A. D. Stone, and L. Jiang, Quantum Noise Theory of Exceptional Point Amplifying Sensors, *Phys. Rev. Lett.* **123**, 180501 (2019).
- [110] C. Chen, L. Jin, and R.-B. Liu, Sensitivity of parameter estimation near the exceptional point of a non-Hermitian system, *New J. Phys.* **21**, 083002 (2019).
- [111] J. Naikoo, R. W. Chhajlany, and J. Kolodynski, Multiparameter Estimation Perspective on Non-Hermitian Singularity-Enhanced Sensing, *Phys. Rev. Lett.* **131**, 220801 (2023)
- [112] H. Loughlin and V. Sudhir, Exceptional-Point Sensors Offer No Fundamental Signal-to-Noise Ratio Enhancement, *Phys. Rev. Lett.* **132**, 243601 (2024).
- [113] E. J. Bergholtz, J. C. Budich, F. K. Kunst, Exceptional Topology of Non-Hermitian Systems, *Rev. Mod. Phys.* **93**, 15005 (2021)
- [114] Y. Ashida, Z. Gong, and M. Ueda, Non-Hermitian Physics, *Adv. Phys.* **69**, 3 (2020).
- [115] M. S. Ergoktas et al., Topological engineering of terahertz light using electrically tunable exceptional point singularities, *Science* **376**, 184 (2022).
- [116] J. Peřina, Jr., A. Miranowicz, J. K. Kalaga, and W. Leoński, Unavoidability of nonclassicality loss in \mathcal{PT} -symmetric systems, *Phys. Rev. A* **108**, 033512 (2023).
- [117] R. Wakefield, A. Laing, and Y. N. Joglekar, Non-Hermiticity in quantum nonlinear optics through symplectic transformations, *Appl. Phys. Lett.* **124**, 201103 (2024).
- [118] J. Peřina, Jr., K. Thapliyal, G. Chimczak, A. Kowalewska-Kudłaszyk, and A. Miranowicz, Multiple quantum exceptional, diabolical, and hybrid points in multimode bosonic systems: II. Nonconventional \mathcal{PT} -symmetric dynamics and unidirectional coupling, e-print arXiv:2405.01667 (2024).
- [119] K. Thapliyal, J. Peřina, Jr., G. Chimczak, A. Kowalewska-Kudłaszyk, and A. Miranowicz, Multiple quantum exceptional, diabolical, and hybrid points in multimode bosonic systems: I. Inherited and genuine singularities, e-print arXiv:2405.01666 (2024).
- [120] P. Egenlauf, P. Rommel, J. Main, Gaussian-process-regression-based method for the localization of exceptional points in complex resonance spectra, *Mach. Learn.: Sci. Technol.* **5**, 015045 (2024).
- [121] M. P. Almeida, F. de Melo, M. Hor-Meyll, A. Salles, S. P. Walborn, P. H. Souto Ribeiro, and L. Davidovich, Environment-Induced Sudden Death of Entanglement, *Science* **316**, 579 (2007).
- [122] Jhen-Dong Lin, Po-Chen Kuo, Neill Lambert, Adam Miranowicz, Franco Nori, Yueh-Nan Chen, Non-Markovian Quantum Exceptional Points, arXiv:2406.18362.
- [123] N. Lambert, S. Ahmed, M. Cirio, and F. Nori, Modelling the ultra-strongly coupled spin-boson model with unphysical modes, *Nat. Commun.* **10**, 3721 (2019).
- [124] S. Axler, *Linear Algebra Done Right* (Springer, New York, 2015).
- [125] A. Miranowicz, K. Bartkiewicz, J. Peřina Jr., M. Koashi, N. Imoto, and F. Nori, Optimal two-qubit tomography based on local and global measurements: Maximal robustness against errors as described by condition numbers, *Phys. Rev. A* **90**, 062123 (2014).
- [126] K. Bartkiewicz, A. Černoch, K. Lemr, A. Miranowicz, Priority Choice Experimental Two-qubit Tomography: Measuring One by One All Elements of Density Matrices, *Sci. Rep.* **6**, 19610 (2016).
- [127] A. Miranowicz, S. K. Özdemir, J. Bajer, G. Yusa, N. Imoto, Y. Hirayama, and F. Nori, Quantum state tomography of large nuclear spins in a semiconductor quantum well: Optimal robustness against errors as quantified by condition numbers, *Phys. Rev. B* **92**, 075312 (2015).
- [128] M. Kopciuch, M. Smolis, A. Miranowicz, and S. Pustelný, Optimized experimental optical tomography of quantum states of room-temperature alkali-metal vapor, *Phys. Rev. A* **109**, 032402 (2024),
- [129] A. Possolo, Simple Guide for Evaluating and Expressing the Uncertainty of NIST Measurement Results, NIST Technical Note 1900 (2015), DOI:10.6028/NIST.TN.1900.

ACKNOWLEDGEMENTS

The authors thank Anna Kowalewska-Kudłaszyk, Grzegorz Chimczak, and Jan Peřina for insightful and useful discussions. Our experiments were conducted on the IBM Quantum Network through the IBM Quantum Hub operated by the Poznań

Supercomputing and Networking Center (PSNC). The views expressed are those of the authors, and do not reflect the official policy or position of IBM or the IBM Quantum team. This work was supported by the Polish National Science Centre (NCN) under the Maestro Grant No. DEC-2019/34/A/ST2/00081. S.K.Ö. acknowledges support from Air Force Office of Scientific Research (AFOSR) Multidisciplinary University Research Initiative (MURI) Award on Programmable systems with non-Hermitian quantum dynamics (Award No. FA9550-21-1-0202).

COMPETING INTERESTS

The authors declare no competing interests.

ADDITIONAL INFORMATION

Supplemental document. See Supplement 1, which includes Ref. [124], for the derivations of the transformation matrices for the three equivalent QPT methods.